Diverse bacterial pattern recognition receptors sense the conserved phage proteome

Hyunbin Lee*[1,2], Sofia Luengo-Woods*[1,2], Jianxiu Zhang*[3], Kira S. Makarova[4], Yuri I. Wolf[4], Collin Chiu[1,2], Simone A. Evans[1,2,5], Junyi Chen[1,6], Haopeng Xiao[1,6], Liang Feng[3], Eugene V. Koonin[4], Alex Gao[1,2] ✉

[1]Department of Biochemistry, [2]Department of Microbiology and Immunology, [3]Department of Molecular and Cellular Physiology, Stanford University, Stanford, CA 94305, USA, [4]Computational Biology Branch, Division of Intramural Research, National Library of Medicine, National Institutes of Health, Bethesda, MD 20894, USA, [5]Department of Genetics, [6]Stanford Cancer Institute, Stanford University, Stanford, CA 94305, USA, *Equal contributions

Recognition of foreign molecules inside cells is critical for immunity in all domains of life. Proteins of the STAND NTPase superfamily, including eukaryotic nucleotide-binding oligomerization domain (NOD)-like receptors (NLRs), play a central role in this process. In bacteria and archaea, although several STAND NTPase families have been reported to sense phage proteins, their functional diversity remains largely unexplored. Here, we conducted a systematic phylogenetic analysis of prokaryotic STAND NTPases and identified at least 90 structurally distinct families associated with antiviral defense. We first show that the uncharacterized Avs7 family recognizes the major capsid protein (MCP) of tailed phages. Three cryo-EM structures of *Salmonella enterica* Avs7 reveal an asymmetric, butterfly-shaped tetramer that assembles stepwise via large, MCP-induced conformational changes, incorporating bacterial translation elongation factor Tu (EF-Tu) as a scaffold that is required for full defense activity. Using highly parallel genetic screens, we further show that 13 additional STAND families sense 12 conserved phage protein folds, encompassing most of the core structural and replicative components of tailed phages. These include two structurally distinct families—Avs8 (PD-λ-4) and Avs10 (Erebus/Hypnos/bNACHT64)—that also recognize MCP, as well as 11 other families (Avs11–21) that recognize the portal, portal adaptor, tail nozzle, head–tail connector, tail terminator, tail tube protein, tail assembly chaperone, tape measure protein, DNA polymerase, helicase/RecA-type ATPase, and single-stranded DNA annealing protein (SSAP), respectively. Together, our findings highlight structure-based pattern recognition and host factor repurposing as fundamental strategies of bacterial immunity.

Correspondence: ***algao@stanford.edu***

Introduction. The ability to detect and respond to foreign molecules inside the cell is a fundamental mechanism of immunity across all domains of life. In animals, plants, and fungi, intracellular NOD-like receptors (NLRs)—members of the STAND (Signal Transduction ATPases with Numerous Domains) superfamily of NTPases—play a central role in this process[1,2]. NLRs typically have a tripartite domain architecture consisting of a central NTPase domain, a C-terminal sensor, and an N-terminal effector. These receptors sense pathogen-associated molecular patterns (PAMPs) and oligomerize to initiate inflammation or programmed cell death[3]. In animals, examples include NAIP, which detects bacterial flagellin and type 3 secretion systems[4,5], and NOD1/2, which sense peptidoglycan fragments from the bacterial cell wall[6,7]. NLRs are critical for immune function, with mutations leading to diseases such as potato late blight, bacterial liver infections in mice, and MIRAGE syndrome in humans[3,8].

STAND superfamily proteins are also abundant in bacteria and archaea[1,2], and some of them, which we termed antiviral STANDs (Avs), provide protection against phage infection[9]. We previously demonstrated that four families, Avs1–4, recognize the folds of two conserved proteins, large terminase subunit and portal, through direct binding[10]. Recent studies have shown other STAND activation mechanisms, including the recognition of multiple proteins by a single sensor[11] and sensing of host chaperone perturbation[12]. Several additional STAND families have been reported[9,13–16] or predicted[17] to confer anti-phage protection[9,13–16], and one branch—the NACHT clade—has been systematically analyzed computationally[15], but on the whole, the vast repertoire of prokaryotic STANDs remains poorly characterized. We undertook a systematic study of these proteins, which could be expected to reveal a wide array of distinct defense activation mechanisms in prokaryotes.

Here, we present a large-scale computational and experimental analysis of STANDs across bacteria and archaea. Our computational mining pipeline identified 198 defense-associated STAND clades, encompassing at least 90 structurally distinct sensor architectures. Among these, we describe a previously uncharacterized family, Avs7, that detects the major capsid protein (MCP) of tailed phages. To elucidate its activation mechanism, we determined cryo-electron microscopy (cryo-EM) structures of *Salmonella enterica* Avs7 (SeAvs7) in three states: the inactive apo monomer, the intermediate monomeric complex, and the assembled tetrameric complex, with the latter two bound to MCP from *Escherichia* phage ZL19. MCP binding triggers extensive conformational changes in apo SeAvs7 that drive assembly of the active tetramer, which incorporates translation elongation factor Tu (EF-Tu) as a structural scaffold. To further characterize diverse STAND families, we conducted highly parallel genetic screens, identifying 13 families (Avs8 and Avs10–21) that are activated by the folds of conserved phage proteins, covering nearly all of the core structural and replicative components of tailed phages.

Systematic analysis of defense-associated STAND proteins in prokaryotes. STAND NTPase domains are highly divergent and share conserved motifs with function-

ally diverse AAA+ ATPases, most of which are involved in processes unrelated to immunity[18], complicating systematic identification of defense-associated STANDs. To systematically capture the diversity of defense-associated STAND proteins, we used a two-step, systematic approach (Fig. 1a). We first identified a set of 656 "seed" STAND proteins, including known immune-related STANDs[2,9,15,16,19] and new candidates we detected by their localization in genomic proximity to other defense-related genes (Supplementary Table 1)[9,20,21]. We then performed relaxed PSI-BLAST searches using the conserved NTPase domains of these seeds as queries, and after several rounds of curation (see Methods), expanded the set to 359,879 diverse representatives (clustered at 75% sequence identity) distributed across 589 STAND clades (Fig. 1b and Supplementary Table 2; see Methods). These sequences included known animal and plant NLRs, even though many of these were not included among the seeds, supporting the sensitivity of this approach.

We classified 198 of the 589 clades as defense-associated based on their proximity to known defense systems and/or the presence of a defense-related effector domain (see Methods; Fig. 1a, Supplementary Fig. 1a, Supplementary Tables 3–4). Notably, our analysis identified CRISPR-associated STANDs (clades 324 and 327)[22] and prophage-encoded STANDs (clades 260 and 534)[23], consistent with their established roles in anti-phage defense (Supplementary Fig. 1b–c). Defense-associated clades are intermingled with non-defense STAND clades, suggestive of multiple functional changes throughout the evolution of the STAND superfamily (Fig. 1b). Known NLRs from animals[24–28], plants[29,30], and bacteria[9,10,14–16] were found in distinct clades, alongside non-immune STANDs such as transcriptional regulators[31–34], the telomerase-associated protein TEP1, and the primary cilia protein NPHP3, consistent with earlier analyses[2,35].

Given the large size of STANDs among defense proteins (Supplementary Fig. 1e), we explored the diversity of the C-terminal sensor domains by grouping larger defense-associated sensors ($\geq$ 400 amino acids) into 684 clusters by sequence and structural similarity (Supplementary Fig. 2a–e and Supplementary Table 5). Most defense-associated clades were dominated by a single sensor type (Supplementary Fig. 2f). Analysis of the 90 most prevalent clusters revealed contrasting evolutionary patterns: some were clade-specific (e.g. Avs2), whereas others spanned multiple clades (e.g. sensor structural cluster 39; Fig. 1c–e, Supplementary Fig. 2–5). The majority of the sensors were composed of TPR-like α-helical repeats (Fig. 1c, Supplementary Fig. 3, 4a–b, and 5), although we also identified other types, including WD40 β-propeller repeats and formylglycine-generating enzyme (FGE) sulfatase-like domains (Fig. 1d–e, Supplementary Fig. 4c–d). This diversity mirrors the sensor repertoire of eukaryotic NLRs[3].

Notably, we identified specific structural similarity between several bacterial sensors and animal proteins involved in immunity. The Avs5 sensor clustered with the SAMD9 family of animal antiviral restriction factors, consistent with recent observations[17] and the conservation of certain immune functions between prokaryotes and eukaryotes (Supplementary Fig. 4b)[36]. We also detected bacterial orthologs of Apaf-1, the core component of the eukaryotic apoptosome[28,37]. Both bacterial and human Apaf-1 share structurally similar β-propeller sensors consisting of WD40 repeats (Fig. 1e and Supplementary Fig. 3b). Several bacterial variants encode an N-terminal caspase-like protease in place of the eukaryotic CARD domain that recruits procaspase-9, suggesting a more direct activation mechanism than that in the animal counterparts. The closest Apaf-1 homologs were found in cyanobacteria, consistent with observed parallels between the defense systems in multicellular bacteria and eukaryotic immunity[38].

A shared sensor domain in Avs7 and Dsr1 recognizes phage major capsid proteins. We first selected for biochemical analysis an uncharacterized STAND family, Avs7, given the consistent presence of its sensor domain, consisting of TPR repeats, across multiple STAND clades (Supplementary Fig. 2i, 3b, and Supplementary Table 6). A comprehensive search for Avs7 homologs in the NCBI nonredundant (nr) protein sequence database revealed their wide distribution across bacterial and archaeal phyla, with each homolog containing one of at least 20 distinct effector domains at its N-terminus (Supplementary Fig. 6 and Supplementary Table 7). The lack of correlation between Avs7 sequences and host phylogenies suggests extensive horizontal gene transfer, a hallmark of immunity-associated STANDs, as well as many other defense genes[2,10].

Unexpectedly, searches with the Avs7 sensor domain alone retrieved proteins in otherwise unrelated defense systems, including defense-associated sirtuin 1 (Dsr1)[9] (Fig. 2a and Supplementary Table 8). These proteins lack the STAND NTPase domain and contain diverse effectors such as NADases, nucleases, and protein kinases. AlphaFold3 models of *Salmonella enterica* Avs7 (SeAvs7), *Escherichia coli* Dsr1 (EcDsr1), and a *Streptomyces* HEPN-containing protein all showed a conserved bilobed architecture formed by a sharply bent sensor region consisting of multiple TPR repeats (Supplementary Fig. 7). Phylogenetic analysis of the sensor domains placed Avs7 and Dsr1 in two distinct clades, with some intermixing that might reflect effector exchange during evolution (Fig. 2a).

SeAvs7 conferred robust defense in *E. coli* against 9 *Drexlerviridae* family coliphages, including ZL19 and T1, whereas EcDsr1 was active against only a few phages (Fig. 2b and Supplementary Fig. 8a). To identify the triggers of SeAvs7 and EcDsr1, we performed proteomic profiling of T1-infected cells expressing tagged SeAvs7 (Fig. 2c), which revealed significant enrichment of the T1 major capsid protein (MCP; T1 ST47) and the host elongation factor Tu (EcEF-Tu) bound to SeAvs7 compared to a sensor-deleted mutant (Fig. 2c, Supplementary Fig. 8b–e, and Supplementary Table 9). A co-expression toxicity screen using a barcoded library of 73 genes from ZL19 identified MCP as the unique trigger of both SeAvs7- and EcDsr1-mediated cell

death (Fig. 2d–e and Supplementary Table 10), and direct co-expression of ZL19 MCP with SeAvs7 in *E. coli* caused pronounced cell death (Fig. 2f). Together, these results establish MCP as the trigger for Avs7 sensors across distinct defense systems. Disruptions of the N-terminal effector domains abolished both MCP-induced toxicity and defense activity, indicating that defense is mediated by the effectors (Supplementary Fig. 9).

The SeAvs7:MCP complex incorporates elongation factor Tu. To investigate the activation of SeAvs7, we purified SeAvs7 and ZL19 MCP as recombinant proteins and incubated them in vitro (Supplementary Fig. 10a). Size-exclusion chromatography (SEC) showed that these proteins formed a large multimeric complex in the presence of ATP and Mg^{2+} (Fig. 2f and Supplementary Fig. 10b). This complex efficiently degraded double-stranded DNA (dsDNA) substrates, whereas SeAvs7 alone did not (Fig. 2h). EcEF-Tu co-purified with SeAvs7 even in the absence of phage infection and co-eluted with the SeAvs7:ZL19 MCP complex during SEC (Supplementary Fig. 10b). To rule out nonspecific binding, we reconstituted the complex in vitro using individually purified SeAvs7, ZL19 MCP, and EcEF-Tu proteins (Fig. 2f and Supplementary Fig. 10c–d). SEC analysis confirmed that EcEF-Tu was stably incorporated into the multimeric complex at an approximately 1:1:1 molar ratio, demonstrating its role as a core component of the complex (Supplementary Fig. 10e).

To clarify the role of each protein, we assessed nuclease activity across different combinations of the individually purified proteins (Fig. 2f and Supplementary Fig. 10c). DNA degradation required both SeAvs7 and ZL19 MCP and was substantially enhanced by EcEF-Tu (Fig. 2i). Although cleavage occurred without EcEF-Tu after prolonged incubation, the presence of EcEF-Tu notably increased the sensitivity of SeAvs7 to ZL19 MCP (Fig. 2j–k). These findings suggest that EcEF-Tu enhances the defense response by facilitating the recognition of the MCP. Given the high cellular concentration of EF-Tu (comprising 6–10% of the total *E. coli* proteome[39]) and its sequence conservation between *E. coli* and *Salmonella enterica* (differing by only one amino acid at position 190), this enhancer role is likely conserved in the native host. Finally, the elimination of both defense and cellular toxicity of SeAvs7 by inactivation of the Cap4 nuclease indicates that the defense capacity of SeAvs7 is not driven by EF-Tu sequestration (Supplementary Fig. 9b).

Binding of MCP induces SeAvs7 assembly into an active asymmetric tetramer. To understand how ZL19 MCP and EcEF-Tu interact with SeAvs7, we determined the structures of the oligomeric complex by cryo-electron microscopy (cryo-EM) (Fig. 3a–b, Supplementary Fig. 11, and Supplementary Table 11). Refinement revealed two distinct structures: an approximately 1 MDa butterfly-shaped tetrameric complex at 3.43 Å resolution containing four copies each of SeAvs7, ZL19 MCP, and EcEF-Tu, and a smaller ~250 kDa complex at 3.40 Å resolution with a single copy of each protein (Fig. 3a–b). Although the tetrameric complex showed low resolution in the SeAvs7 TPR lobes, local refinement of these regions improved the resolution to 3.70–4.01 Å (Supplementary Fig. 11). The tetrameric complex was asymmetric, with protomers structurally similar except for the orientation of the SeAvs7 Cap4 domain (Fig. 3a and Supplementary Fig. 12). In contrast, the smaller monomeric complex lacked density for the Cap4 nuclease and the N-terminal part of the NTPase, suggesting that these regions are flexible in the monomeric state but are stabilized upon tetramerization (Fig. 3b). The remaining parts—the C-terminal region of the NTPase domain and the sensor—closely resemble a protomer of the tetrameric complex (Supplementary Fig. 12).

Tetramer formation is mediated by the Cap4 and NTPase domains. The Cap4 nuclease tetramer adopts a C2-symmetric arrangement with two inward- and two outward-facing protomers (Fig. 3c). The inward Cap4 protomers contact each other through helix–helix interfaces, whereas the outward protomers engage in close contacts with the inward ones, forming two hydrogen bonds and burying ~12% (~1300 $Å^2$) of their solvent-accessible surface area (Supplementary Fig. 13a–b). This configuration contrasts that of the related SeAvs3 receptor[10] (PDB 8DGC), which buries only ~2% (~280 $Å^2$) of the surface area of its outward Cap4 protomers and adopts a distinct tetrameric arrangement (Supplementary Fig. 13c). Nevertheless, the inward protomers of SeAvs7 resemble those of SeAvs3, and AlphaFold3 modeling placed dsDNA in the PD-(D/E)xK active site of Cap4 (Supplementary Fig. 13d), indicating that these protomers are accessible for DNA binding and likely form the active nuclease. Finally, Cap4 regulation differs between the two receptors. In SeAvs3, a flexible loop (residues 41–60) occludes DNA binding in the outward-facing protomers. In SeAvs7, the equivalent loop (residues 37–45) is too short; instead, another extended loop (residues 199–215) blocks the outward-facing protomers, and α-helices from adjacent protomers restrict access to the inward active sites (Fig. 3c).

The overall asymmetry of the SeAvs7 complex is established via close contacts between the NTPase domains of adjacent protomers (Fig. 3d). A flexible 10-residue loop between the Cap4 and the NTPase domains enables the symmetry mismatch between them. Although the NTPase tetramer could in principle accommodate a fifth protomer, it is unnecessary for Cap4 assembly (Supplementary Fig. 14a), and pentamers were not observed under conditions favoring complex formation. Together with the functional role of the Cap4 tetramer, these findings indicate that the asymmetric tetramer represents the fully assembled immune complex rather than a partial intermediate.

The STAND NTPase domain consists of three subdomains: the nucleotide-binding domain (NBD), winged-helix domain (WHD), and helical domain 1 (HD1). The NBD and WHD of adjacent protomers form three hydrogen bonds across a ~1,100 $Å^2$ interface, while HD1 lies outside the main interface (Supplementary Fig. 14b–c). Each protomer coor-

dinates ATP and Mg^{2+} through conserved residues (Thr291, Lys292, Asp358, and Arg395), consistent with the previously characterized active conformations of other STAND NTPase oligomers (Supplementary Fig. 14d)[10,25,27,28,30,40].

The TPR sensor of SeAvs7 adopts a bilobed structure that envelops the ZL19 MCP, burying 3,700 $Å^2$ of its 15,800 $Å^2$ solvent-accessible surface (Fig. 3e). Binding is driven by the shape and charge complementarity between the sensor and the HK97-fold of MCP, including the peripheral (P) domain, axial (A) domain, and extended loop (E-loop; Fig. 3f)[41–43]. The sensor extensively engages with the conserved penton/hexon-forming region of the A-domain, while making surface contacts with the variable P-domain and E-loop (Fig. 3f)[41,42,44,45]. A broad interface centered on a conserved region appears to be a general feature of Avs7 sensors, as also predicted for other Avs7–MCP pairs by AlphaFold3 (ref.[46]) (Supplementary Fig. 15a). Although we identified five residues potentially involved in hydrogen bond network formation, mutating three of these (N1204, Y1289, and N1361) did not abolish defense against ZL19, suggesting that recognition depends on extensive structural complementarity rather than on a few specific contacts (Supplementary Fig. 15b–c).

EF-Tu binding enhances complex assembly, nuclease activity, and defense. While ZL19 MCP is enveloped by the TPR sensor of SeAvs7, EcEF-Tu binds the outer surface of the flexible sensor region and adjacent helices through its tRNA-binding domains (Domain II and Domain III), burying ~1,450 $Å^2$ of solvent-accessible surface (Fig. 4a)[47,48]. The interaction is also facilitated by shape and charge complementarity (Fig. 3f). The bound EcEF-Tu adopts the inactive, open state typically bound to GDP (Supplementary Fig. 16a), although our cryo-EM map could not resolve the identity of the bound nucleotide. Structural superposition suggests that the closed, active state, which favors GTP, would be sterically blocked by clashes with the TPR N-lobe (Supplementary Fig. 16b)[47,49].

To gain insight into the importance of EcEF-Tu binding for Avs7 functionality, we analyzed the SeAvs7:EcEF-Tu interface and mapped the contacting residues to the Avs7 multiple sequence alignment (Fig. 4a and Supplementary Fig. 17). Several of these residues are conserved within one Avs7 clade (Supplementary Fig. 17a-b). Consistent with this observation, AlphaFold3 confidently predicted Avs7:MCP:EF-Tu-like complexes exclusively from this clade, suggesting clade-specific conservation of the Avs7:EF-Tu interaction (Supplementary Fig. 17c–d and Supplementary Table 12). To test the functional importance of the interaction, we generated four SeAvs7 mutants targeting conserved charged residues (Q999, D1003, K1044, H1048, D1059; Fig. 4a and Supplementary Fig. 17a–b). None of these mutants co-purified with detectable amounts of EcEF-Tu when expressed alone, indicating substantially reduced affinity (Fig. 4b). Upon reconstitution of the multimeric complex, mutants II-1 ($SeAvs7^{Q999A/D1003A}$) and II-2 ($SeAvs7^{Q999A/D1003K}$) formed EF-Tu-containing complexes at levels comparable to WT; mutant III-1 ($SeAvs7^{K1044A/H1048A/D1059A}$) formed less complex; and mutant III-2 ($SeAvs7^{K1044E/H1048D/D1059K}$) failed to incorporate a detectable amount of EcEF-Tu (Fig. 4c). EF-Tu-mediated enhancement of nuclease activity directly paralleled this assembly efficiency, with WT and mutant II-1 strongly enhanced, and mutants II-2, III-1, and III-2 showing progressively weaker effects (Fig. 4d). Plaque assays against nine *Drexlerviridae* family phages (with pairwise sequence identities of MCPs ranging from 48.9% to 97.5%) further corroborated the functional link, showing progressive loss of defense from mutant II-1 to III-2 against five phages, mirroring the trends in complex formation efficiency and nuclease activity enhancement (Fig. 4e and Supplementary Fig. 18). The loss of defense activity by the most disruptive mutant (III-2) did not correlate with either MCP sequence similarity or phage phylogeny, indicating the promiscuity and varied dispensability of Avs7:EF-Tu interaction across the diversity of phages (Fig. 4e). Together, these findings establish EcEF-Tu as a key partner of Avs7 that optimizes phage defense by promoting the formation of the complex between Avs7 and phage MCP, and enhancing nuclease activity.

MCP binding triggers structural rearrangements for SeAvs7 oligomerization. To understand the molecular basis of SeAvs7 activation, we determined the structure of apo SeAvs7 at 2.72 Å resolution (Fig. 5a, Supplementary Fig. 19, and Supplementary Table 11). Although EcEF-Tu co-purified with SeAvs7, no corresponding cryo-EM density was observed, suggesting weak association in the absence of MCP (Supplementary Fig. 19a). Relative to the tetrameric complex, the apo structure shows a ~90° rotation of the NBD and HD1 with respect to the WHD, and none of these domains are resolved in the monomeric complex (Fig. 5b). Notably, ADP occupies the NTPase active site and stabilizes a closed conformation, despite ATP being supplied during purification (Supplementary Fig. 20a). In contrast, the tetrameric complex contains exclusively ATP, suggesting ADP-to-ATP exchange during activation. Recognition of both nucleotides involves largely the same residues, with the exception of an Arg395–ATP γ-phosphate contact replacing a His545–ADP β-phosphate contact (Supplementary Fig. 20a). Consistent with this distinction, DNA cleavage was slower in the presence of ADP or the nonhydrolyzable ATP analog adenylyl-imidodiphosphate (AMP-PNP), and absent without a nucleotide, indicating that nucleotide binding promotes activation through a conformational change rather than through ATP hydrolysis (Supplementary Fig. 20b).

The apo state of SeAvs7 is maintained by extensive autoinhibitory interactions. The closed conformation of the NTPase is stabilized by its interaction with the C-lobe through charge complementarity and a network of hydrogen bonds around a partially conserved Arg367 (Supplementary Fig. 21a–b). The Cap4 nuclease domain is prevented from oligomerizing by forming extensive hydrogen bond networks with the NBD and engaging the C-lobe (Supplementary Fig. 21b–c). Structural superposition reveals steric clashes between the Cap4

tetramer and the C-lobe of apoSeAvs7, indicating tetramerization is incompatible with the apo conformation (Supplementary Fig. 21d).

Binding of ZL19 MCP triggers global conformational changes that relieve autoinhibition of SeAvs7. Superimposing the apo and tetramer structures by the WHD shows that MCP binding causes the TPR N- and C-lobes to move towards each other, displacing one by ~30 Å relative to the other (Fig. 5c and Supplementary Fig. 22a). This movement leads to steric clashes between the MCP-bound C-lobe and the NTPase helices of the apo form, likely disrupting the interactions that stabilize the inactive state (Fig. 5d). These include a notable clash between the last helix of the C-lobe (residues 1511–1521) and two helices in the NBD (residues 360–367 and 396–401) in apo SeAvs7. The C-terminal helix is present and has a conserved length across Avs7 homologs (Supplementary Fig. 22b).

Based on these observations, we propose a stepwise mechanism for the activation and assembly of Avs7 complexes (Fig. 5e). In the absence of MCP, Avs7 remains in an autoinhibited, ADP-bound resting state. Upon phage infection, the Avs7 sensor binds a newly synthesized MCP monomer, strengthened by EF-Tu, clamping the two lobes of the sensor. These conformational changes destabilize the ADP-bound state of the NTPase, likely promoting ADP release and increased flexibility of the N-terminal domains. Finally, ATP binding stabilizes the NTPase, driving tetramerization and enabling Cap4-mediated DNA cleavage to prevent phage replication.

Thirteen additional Avs families are activated by diverse phage proteins. Given the extensive diversity of bacterial Avs proteins, we hypothesized that other Avs families could be activated by different phage proteins. To investigate the diversity of Avs sensor domains, we selected representative proteins from 27 additional sensor structural clusters. We focused on those from bacteria within the family *Enterobacteriaceae* because these are more likely to be successfully reconstituted in *E. coli* (Supplementary Fig. 2g and 2i, Supplementary Table 6). To identify the triggers of these Avs families, we conducted an expanded genetic screen with 600 genes from 36 diverse phages and viruses (totaling 521 kb), including ssRNA, ssDNA, and tailed and tail-less dsDNA phages[50] cloned into barcoded plasmids (Fig. 6a and Supplementary Table 10). After transforming the constructed library into *E. coli* strains expressing each of the tested Avs representatives, we performed deep sequencing on the resulting barcode pool to quantify cell death in response to phage gene expression (Fig. 6a).

Thirteen additional families, which we denoted Avs8 and Avs10–21 (since Avs6 and Avs9 now refer to other SAMD9-like STAND families[17]), were found to strongly induce cell death in response to specific phage proteins (Fig. 6b and Supplementary Fig. 24). Each of these families was consistently triggered by orthologous proteins from different phages. Remarkably, the diverse set of Avs activators encompassed the core structural proteins of tailed phages[51], as well as four key non-structural proteins involved in phage genome replication. Specifically, Avs8 (PD-λ-4)[13] and Avs10 (Erebus/Hypnos/bNACHT64)[15,16] were activated by MCP, whereas Avs12-18 were activated by seven proteins of the phage structural module: portal adaptor, tail nozzle, head-tail connector, tail terminator, tail tube protein (TTP), tail assembly chaperone (TAC), and tape measure protein (TMP), respectively (Fig. 6b). Our Avs8 findings are consistent with a recent preprint by Nagy et al.[52] In contrast, Avs19–21 were activated by replicative proteins: DNA polymerase, the RecA-type ATPase domain in both the primase-helicase and RecA, and single-stranded DNA annealing protein (SSAP), respectively (Fig. 6b). Avs11 recognized the portal protein despite lacking sequence and structural similarity to the previously characterized portal-sensing Avs4 (Fig. 6b and Supplementary Fig. 3). In all cases, mutations or deletions of the effector domains abolished cell death-inducing activity (Supplementary Fig. 25).

To evaluate the specificity of Avs target recognition, we cloned 6 or more homologs of each Avs target protein from diverse phages, spanning all three major structural classes of tailed phages, totaling 218 genes (Supplementary Table 13). We then tested all these phage proteins with 18 Avs7–8 and Avs10–21 representatives, using Avs2 and Avs3 as positive controls, and quantified all 4,360 pairwise interactions by deep sequencing. Each Avs protein was specific for its cognate target protein, with minimal cross-reactivity to other targets, in agreement with our initial genetic screen (Fig. 6c and Supplementary Fig. 26). Within each target family, however, a broad range of homologs was recognized, some with no significant sequence similarity, but sharing the same core fold (Supplementary Fig. 27–28). EcAvs19 appeared to prefer family A DNA polymerases from diverse phages, while not recognizing the endogenous *E. coli* family A DNA polymerase I (ref.[53]) (Supplementary Fig. 28c). The SSAP sensor Avs21 could detect both ERF-family and RecT-family SSAPs (Supplementary Fig. 28d), which share a core fold but virtually no sequence similarity[54]. The conservation of Avs target proteins (Fig. 6d) mirrors their overall synteny of structural genes across phage genomes (Supplementary Fig. 23).

To further validate the genetic activation results, we assessed the anti-phage activity of the tested Avs families in *E. coli* against a panel of 12 diverse phages (Supplementary Fig. 29–30). Most of these families displayed anti-phage activity, with phage specificities generally aligning with the co-expression toxicity results. Anti-phage activity was also detected for four additional sensor structural clusters (Avs22–24 and bNACHT20) for which no phage-encoded activators were identified in co-expression toxicity assays (Supplementary Fig. 29–30). Further investigation is needed to determine how these Avs families sense phage infection.

Avs proteins recognize core phage structural patterns. To determine how the 13 additional Avs families recognize their cognate target proteins, we generated AlphaFold3 or AlphaFold-multimer models for each Avs–target com-

plex and tested these models using truncation and mutational analyses in *E. coli*. We obtained confident predictions (ipTM 0.71-0.91) for 11 of the 13 complexes (Fig. 7 and Supplementary Fig. 31–32). In each case, the Avs TPR-like helical sensor was bound to a single copy of the target protein through an extensive shape-complementary interface. In vitro reconstitution of two of the 11 complexes (KpAvs20:HdK1 RecA and MvAvs13:PhiV-1 tail nozzle) with purified proteins validated the binding between these Avs and their respective target phage proteins (Fig. 7b, d).

The Avs sensors consistently recognized the conserved core fold of their targets, leaving variable extensions and insertions generally unbound (Supplementary Fig. 27–28). Although the overall structures of the sensors of Avs7, Avs8, and Avs10 differ, they all recognize the penton-/hexon-forming interface of the A-domain of MCP (Fig. 7e). The TPR-like sensors of Avs12, Avs14, and Avs15 envelop the globular folds of their single-domain targets: the portal adaptor, head-tail connector, and tail terminator, respectively (Fig. 7f–h)[55]. The Avs16 sensor forms extensive contacts with the conserved β-hairpin of the tail tube protein, which constitutes the interface between stacked hexameric rings of the tail tube (Fig. 7i). In contrast, the Avs13 sensor forms a large circular structure that surrounds the tail nozzle protein of podophages (Fig. 7c). The Avs17 sensor binds to the N-terminal core of the TAC, a region shared by both long and short TAC isoforms generated through internal programmed translational frameshift (e.g. gpG and gpGT from phage lambda[56]) (Fig. 7j). Structural models of the SeAvs18:TMP complexes suggest that its sensor binds to a central ~130-residue α-helical segment of TMPs, which we identified as the most conserved region using PROMALS3D[57]. This segment was necessary and sufficient for activating cell death (Fig. 7k and Supplementary Fig. 27c, 31f). Finally, core folds of replicative proteins were also recognized: the Avs20 sensor recognizes the RecA-type ATPase domain of both the primase-helicase and RecA[58], independent of the ATPase activity (Fig. 7a), and the Avs21 sensor binds to the N-terminal ssDNA-binding domain of both ERF-family and RecT-family SSAPs (Fig. 7l).

While high-confidence models could not be generated for CkAvs11–portal and EcAvs19–DNA polymerase complexes, predictions of apo Avs proteins suggest autoinhibition that might be released by target binding (Supplementary Fig. 31i, j). The core polymerase domain was necessary and sufficient to activate EcAvs19, independent of the polymerase catalytic aspartate (Fig. 7m).

Altogether, our structural modeling and mutational analyses consistently demonstrate that Avs receptors recognize conserved core folds in highly divergent target proteins (Fig. 7 and Supplementary Fig. 31). Notably, this recognition mechanism apparently targets monomers of these proteins, as our models showed significant steric clashes with oligomerized or substrate-bound forms (Supplementary Fig. 33).

Discussion. Here we present a systematic study of the diversity and activation of prokaryotic STAND defense systems, demonstrating that the conserved core folds of nearly all core proteins of tailed phages are targeted by dedicated Avs. By focusing on a widespread family, Avs7, we elucidate a stepwise assembly mechanism in which, upon MCP binding, the receptor transitions from an autoinhibited resting state to an assembled tetramer via an intermediate monomeric complex. Notably, we identified EF-Tu as an essential host factor that is co-opted by Avs7 for complex assembly and robust defense.

Although several defense systems have been previously shown to bind phage proteins[10,59–65], Avs sensors are distinct in their ability to recognize conserved protein folds through shape-complementary interfaces. This mechanism provides a robust defense strategy that is difficult for phages to evade without compromising their fitness due to disruption of essential protein structures. The widespread distribution of these Avs families among bacteria and archaea suggests that fold sensing is a major, yet underappreciated, mode of antiviral defense in prokaryotes. Our findings identified Avs targets that span nearly all highly conserved core proteins in tailed phages[66], with the HK97-fold MCP being the target of three prevalent families (Avs7, Avs8, and Avs10). Other defense systems also recognize MCP, such as Lit protease[67,68] and CapRel[60,69]; however, unlike Avs7–8 and Avs10, these systems detect short sequence motifs rather than recognizing folds through broad structural complementarity.

Six of the 13 identified targets—tail nozzle, portal adaptor, head-tail connector, tail terminator, tail assembly chaperone, and tape measure protein—have not been previously known to be targeted by antiviral defense. For another three—primase-helicase, RecA, and SSAP—defense escape mutations have been previously identified[65,70–72], but the mechanisms of sensing remain unknown and in many cases could be indirect. Altogether, our findings substantially expand the repertoire of phage proteins that directly activate prokaryotic defense systems.

Our study reveals a previously unknown mechanism of host factor repurposing in anti-phage defense. The scaffolding role of EF-Tu in the Avs7 complex contrasts with its involvement in the functioning of other defense systems such as Lit protease[59,73,74] and type IV Thoeris[75], where EF-Tu is cleaved, resulting in translation arrest. Instead, this mechanism is reminiscent of the ribosomal protein S15 in the type V-K CRISPR-associated transposon (CAST) complex[76], which facilitates DNA mobilization. Another relevant case of EF-Tu repurposing is its recruitment (along with EF-Ts) as an accessory subunit of the RNA-dependent RNA polymerase of RNA bacteriophages of the family *Leviviridae*[77,78]. By recruiting these highly abundant and evolutionarily conserved host proteins, both defense systems and mobile elements appear to achieve a reduction in their own protein investment without substantially perturbing the host proteome[79]. These observations also parallel those for several eukaryotic NLRs that bind host factors, undergoing spatial or conformational changes upon infection[29,80]. Alternatively or additionally, given that T4 MCP binds EF-Tu[74], Avs7 might have evolved to exploit a pre-existing interaction between certain MCPs

and EF-Tu, a mechanism that parallels sensing of DnaJ perturbation by bNACHT25 (ref.[12]).

Our findings do not exclude the existence of other, non-canonical activating mechanisms for the Avs families described here. Alternative activators have been identified for CapRel[69] and for Avs2 (ref.[11]). Avs activation also might require unexpected host factors beyond their phage target, as exemplified by the EF-Tu scaffolding for Avs7 and DnaJ perturbation for bNACHT25 (ref.[12]). Further studies are required to elucidate the full repertoire of these activation mechanisms. Nonetheless, the conservation and structural complementarity of the identified targets with the Avs sensor domains suggest these targets are favored during the host-virus arms race, enabling the sensing of a broad range of phages while avoiding autoimmunity.

Beyond their fundamental role in phage defense, Avs receptors also offer insights for therapeutic phage development and novel antimicrobial strategies, as many antibiotic-resistant clinical bacterial isolates encode these receptors. The identification of target proteins for 14 Avs families—and more broadly, the activation of bacterial defense systems by conserved phage proteins—could offer insights for the design of off-the-shelf phage therapies. Conversely, the ability of small phage proteins to induce Avs-mediated cell death suggests the possibility of artificially activating these intrinsic bacterial cell death pathways to target pathogenic bacteria. Altogether, our findings reveal that structure-based pattern recognition of the conserved phage proteome is a fundamental defense strategy in prokaryotes, highlighting sophisticated adaptations in the host-virus arms race.

Materials and Methods. *Bioinformatic analysis of STAND NTPases*. To systematically identify defense-related STAND NTPases in prokaryotes, we curated an initial set of 656 diverse STAND 'seed' sequences (Supplementary Table 1). This set included representatives of all previously predicted prokaryotic defense-related STANDs[2,9,15,16,19], covering both NACHT and other clades. We also included additional sequences from GenBank identified through BLAST searches using the known STANDs and the defense-associated effector proteins Cap4, Mrr, Trypco2, and metallo-β-lactamase[10].

The 659 NTP-binding domains within the 656 seed sequences were clustered, aligned, and used as queries in PSI-BLAST[81] searches against the NCBI clustered_nr database (non-redundant proteins clustered at 90% identity and 90% coverage) to identify a preliminary set of homologs. Footprints of these searches were then aligned with the corresponding queries and used in a second round of PSI-BLAST searches against the same database, resulting in the identification of 1,750,195 NTP-binding domains from 1,708,335 proteins. These NTP-binding domains, originating from both prokaryotes and eukaryotes, were clustered using MMSeqs2 (ref.[82]) at 75% identity and 67% coverage, yielding 680,395 clusters.

Representatives of these 680,395 clusters (one from each cluster) were selected and further clustered using MMSeqs2 at 33% identity and 67% coverage, producing 37,834 clusters. Sequences within each new cluster were aligned using MUSCLE5 (ref.[83]) and the resulting 37,834 consensus sequences[84] were aligned using FAMSA[85]. Each character of the aligned consensus sequence was then expanded into a corresponding column of the original cluster MSA, generating a pseudo-MSA of 680,395 representative NTP-binding domain sequences.

A preliminary approximate maximum likelihood tree was reconstructed from these sequences using FastTree[86] with gamma-distributed site rates and the WAG evolutionary model. This tree was cut at a depth of 1.5 from the tips into 17,857 clades. The domain content of the 680,395 sequences across these clades were annotated using PSI-BLAST against the NCBI CD database[87]; clades containing potential defense-related NTPases were identified by the presence of likely sensor and effector domains. This procedure identified 884 potential defense-related clades, totaling 359,879 leaves corresponding to NTP-binding domain sequences. The discarded clades mainly consisted of homologous but distantly related P-loop domains identified by PSI-BLAST, such as ABC transporters, adenylate kinases, and Clp proteases, or were singleton outliers.

This subset of 359,879 leaves was further clustered using MMSeqs2 at 25% identity and 67% coverage, resulting in 2,488 clusters. Each cluster was aligned using MUSCLE5, and the 2,488 consensus sequences were aligned using FAMSA. Each character of the aligned consensus sequence was expanded into a corresponding column of the original cluster MSA, resulting in a pseudo-MSA of 359,879 representative NTP-binding domain sequences. A final approximate maximum likelihood tree was reconstructed from these sequences using FastTree with gamma-distributed site rates and the WAG evolutionary model. The tree was cut at a depth of 2.0 from the tips, yielding 589 final STAND clades (Supplementary Table 2). The tree was visualized using ggtree v3.10.1 in R (ref.[88]).

Each of the 589 STAND clades were classified as defense-associated if either or both of the following criteria were met: the presence of defense effector domains within the protein sequences or statistical enrichment of genomic context adjacent to known defense systems.

- The presence of effector domains was assessed using the following criteria: Clades in which at least 50% of the representative sequences contained previously annotated effector domains (detected by PSI-BLAST using CDD profiles; Supplementary Table 3) were classified as high-confidence defense clades (86 clades), and those with 10–50% of sequences containing these domains were considered low-confidence defense clades (86 clades).
- To assess the genomic context of each STAND clade, we used DefenseFinder[89] to identify known anti-phage

defense genes encoded within 5 kb of representative STAND sequences. For each clade, to determine whether the observed proximity to defense genes was significantly greater than expected by chance, we calculated a *P*-value using the binomial distribution. The null probability was set at 0.0153, which reflects the chance that a randomly selected non-defense gene would be located within 5 kb of a defense system, based on our calculated DefenseFinder statistics. Clades with a *P*-value less than 0.0001 were classified as high-confidence defense-associated clades, resulting in 131 such clades (Supplementary Fig. 1b).

This combined classification scheme yielded 198 high-confidence defense-associated STAND clades (Supplementary Table 4). To assess sensor diversity, sequence clusters within these clades (clustered at 75% identity and 67% coverage; see Fig. 1a, step 3) were expanded, resulting in 178,641 proteins. From these, C-terminal regions following the NTPase domains were extracted, and sequences shorter than 400 amino acids were excluded, yielding 34,990 sequences. These sequences were then clustered using MMseqs2 at 80% coverage and an E-value threshold of 10^{-5}, resulting in 1,479 sequence clusters.

For each sequence cluster, a representative AlphaFold structure was either retrieved from the AlphaFold database (https://alphafold.ebi.ac.uk/)[90,91] or predicted using AlphaFold3 (ref.[46]), using the full protein sequence along with one ADP molecule and one Mg^{2+} ion. Seventeen eukaryotic clusters were excluded, and five clusters did not yield structural models. From the remaining 1,457 representative structures, the C-terminal regions following the NTPase domains were extracted and clustered using Foldseek[92] at 80% coverage, an E-value of 10^{-10}, and a TM-score threshold of 0.40, resulting in 684 structural clusters (Supplementary Table 5). For visualization, 90 sensor structural clusters were selected, based on (1) each cluster containing at least five members, and (2) at least 25% of cluster members belonging to defense-associated STAND clades.

Prophage prediction. Prophage regions were detected using PHASTEST[93].

Bioinformatics analysis of Avs7 and Dsr1. Avs7 homologs (Supplementary Table 7) were identified using PSI-BLAST[94] searches against the NCBI nonredundant (nr) protein sequence database in July 2024. After filtering out truncated sequences and non-Avs7 hits, a final set of 3,272 verified Avs7 sequences was obtained. These sequences were then clustered at 90% identity using MMseqs2, resulting in 1,757 clusters, and one representative from each cluster was selected for subsequent analysis. A multiple sequence alignment (MSA) of these representatives, excluding their variable N-terminal domains, was generated using MAFFT v7.520 (ref.[95]) with global pairwise alignment (--maxiterate 1000 --globalpair). The alignment was trimmed with trimAl 1.2 (ref.[96]) using a gap threshold of 0.25 (-gt 0.25). Phylogenetic trees were constructed from the trimmed MSAs using IQ-TREE 1.6.12 (ref.[97]) with the LG+G4 model and 2000 ultrafast bootstrap replicates (parameters -nstop 500 -safe -nt 4 -bb 2000 -m LG+G4). N-terminal effectors were annotated based on HHpred[98,116] predictions, and taxonomic classifications were retrieved from the NCBI taxonomy database. The tree was visualized using iTOL[99].

To identify additional defense proteins that share the Avs7 sensor domain, PSI-BLAST searches were performed against the NCBI nr protein sequence database downloaded in February 2024. The sensors from two Avs7 representatives (OJX47172.1 and WP_079981830.1) were used as queries for ten and nine iterations, respectively, with a maximum E-value threshold of 0.001 and a minimum sequence coverage of 70%. These searches yielded an initial list of 10,249 proteins. Given the high number of Dsr1 homologs in this list, we conducted an additional PSI-BLAST search using the sensor domain of EcDsr1 (WP_029488749.1) for 16 iterations, which added 45 unique proteins.

A round of curation to remove partial proteins and false positives yielded 9,097 proteins containing an Avs7 sensor domain (Supplementary Table 8). These sensor domains were extracted and clustered at 95% sequence identity and 98% coverage using MMseqs2. An MSA of 4,969 representative sequences was generated using MAFFT v7.525 with global pairwise alignment. The alignment was trimmed by trimAl 1.5 with a gap threshold of 0.25. A phylogenetic tree was constructed from the trimmed alignment using IQ-TREE 2.3.6 (ref.[100]) with the LG+G4 model and 2000 ultrafast bootstrap replicates. Protein domains were predicted using HHPred[101], and for split proteins, adjacent sequences were also analyzed. Taxonomic classifications were retrieved from the NCBI taxonomy database, and the tree was visualized using the R package ggtree v3.10.1.

Cloning. Genes were chemically synthesized (Twist Bioscience or Integrated DNA Technologies) or amplified by polymerase chain reactions from genomic DNA using Q5 (New England Biolabs) or Phusion Flash (ThermoFisher) polymerases. Plasmids were constructed with Gibson assembly and transformed into *E. coli* strains Stbl3 or Mach1 (ThermoFisher). *E. coli* colonies were grown in 1.8 mL Terrific Broth overnight at 37 °C with 100 µg/mL carbenicillin or 25 µg/mL chloramphenicol, as appropriate. Plasmids were isolated using Qiagen miniprep buffers and 96-well DNA & RNA binding plates (Epoch Life Science). The full sequences of all plasmids were verified with Tn5 tagmentation and Illumina sequencing, as previously described[9,102].

STAND NTPases and mutants were cloned into a low-copy pACYC184-like plasmid backbone with a chloramphenicol resistance gene (Supplementary Table 6). For genes from *Enterobacteriaceae*, the native promoter and native DNA sequence was retained in most cases (66 systems), with the exception that the *lac* promoter was used if the gene was separated by less than 50 bp from the preceding open reading frame (ORF) in the genome, or if the promoter could be not synthesized (4 systems). Genes outside of *Enterobacteriaceae* (40 systems) were codon optimized for expression in

E. coli K-12 and cloned after a *lac* promoter.

Phage genes and mutants were cloned downstream of an arabinose-inducible pBAD promoter into a pBR322-like plasmid backbone with an ampicillin resistance gene and a 20 bp barcode sequence unique to each clone. One to three clones for each construct, each with a distinct barcode, were retained for inclusion in the phage gene library (Supplementary Tables 10 and 13).

Phage samples. Phages T4, T5, PhiV-1, P1, Lambda, M13, MS2, Qβ, PhiX, and PR772 were obtained from the American Type Culture Collection (ATCC). Phages HdK1, PTXU04, and PMBT57 were obtained from DSMZ. Phages P12-C5, P3-H4, P2-H4, P2-A2, P3-F6, P11-F7, B1, B3, B5, P2-E7, P2-G4, P3-C8, and P2-A6 were isolated from wastewater treatment samples from Palo Alto, California. Wastewater samples were passed through a 0.22 µm syringe filter (Cytiva Whatman), 10^2-, 10^3-, or 10^4-fold diluted in water, and plated on top agar containing *E. coli* K-12 strains ATCC25404 or BW25113 ΔiscR (ref.[103]), similar to phage plaque assays. After overnight incubation at 37 °C, phages from individual plaques were isolated from the top agar.

Phages used in plaque assays were amplified by incubation at 37 °C with *E. coli* K-12 (ATCC25404) or *E. coli* BW25113 in Terrific Broth at log phase (OD_{600} ~0.2-0.5), without shaking, for up to 12 h or until lysis. Lysates were passed through a 0.22 µm syringe filter, and the filtrate was stored at 4 °C for subsequent use.

Phage plaque assays. *E. coli* BW25113 was used in bacteriophage plaque assays in Fig. 2b and 4e, and Supplementary Fig. 8a, 9b, 9d, 15c, and 18a. *E. coli* K-12 (ATCC 25404) was used in bacteriophage plaque assays in Supplementary Fig. 29, except for those related to Avs21, for which *E. coli* Stbl3 was used instead due to the toxicity of Avs21 expression in *E. coli* K-12 (ATCC25404). *E. coli* cultures were grown to saturation in Terrific Broth at 37 °C with orbital shaking at approximately 220 rpm. To 50 mL top agar (10 g/L tryptone, 5 g/L yeast extract, 10 g/L NaCl, 7 g/L agar) was added chloramphenicol (to a final concentration 25 µg/mL) and 1 mL *E. coli* culture, and the mixture was poured into an empty 15 cm Petri dish and left at room temperature for 10–30 min to solidify. Ten-fold serial dilutions of phage in water were then spotted on each plate, with 3 µL per spot. Plates were incubated at 37 °C for approximately 20 h and photographed with a Nikon D7500 DSLR camera in a dark room above a white backlight. Images were scaled, rotated, cropped, and converted to grayscale using custom ImageJ Macro Language and Python scripts.

SeAvs7 affinity purification. Plasmids encoding N-terminal TwinStrep-tagged SeAvs7 or SeAvs7$^{\Delta 561–1523}$ under an araBAD promoter were transformed into *E. coli* K-12 (ATCC25404) cells. A single colony was inoculated in 20 mL TB with carbenicillin (100 µg/mL) and grown at 37 °C for 16 h. The overnight culture was diluted 1:100 into 2 L fresh TB containing carbenicillin (100 µg/mL) and arabinose (0.2% w/v), and incubated at 37 °C with vigorous shaking for 1.5 h. When OD_{600} reached 0.5–0.8, *Enterobacteria* phage T1 was added at a multiplicity of infection (MOI) of 2, and cultures were incubated at 37 °C for an additional 30 minutes without shaking. Cells were harvested by centrifugation (4,000 rpm, 10 min, 4 °C).

Cell pellets were resuspended in 5 mL of lysis buffer (50 mM Tris-HCl pH 7.5, 0.5 M NaCl, 5 % glycerol, 1 mM ATP, 5 mM $MgCl_2$, 1 mM DTT) and lysed by sonication. Insoluble fractions were removed by centrifugation (20,000 xg, 20 min, 4 °C). Clarified lysate mixed with 100 µL of Strep-Tactin resin, and the resin was washed four times with 1 mL of lysis buffer. Bound proteins were eluted three times with 100 µL elution buffer (0.2 M EPPS pH 8.5, 5 mM desthiobiotin). Eluates were analyzed by SDS-PAGE and mass spectrometry (See Proteomics sample preparation, LC-MS analysis, and Proteomics quantification).

Proteomics sample preparation. Pulldown eluates were digested with Lys-C and trypsin (10 ng/µL each) in 200 mM EPPS pH 8.5 at 37 °C overnight with shaking at 1,200 rpm. Neat acetonitrile was added to each digest to a final concentration of 30% (v/v), and peptides were labeled with 62.5 µg TMTpro-16 reagent[104] for 1 h at 25 °C with shaking at 900 rpm. Twenty percent of each TMT-labeled sample was pooled, acidified, and diluted with 1% formic acid to pH <3 and a final acetonitrile concentration <5%. The combined sample was desalted with StageTips, dried in a SpeedVac, and reconstituted in 5% acetonitrile / 5% formic acid.

LC-MS analysis. A total of 1.3 µg of peptides was analyzed by liquid chromatography–mass spectrometry (LC-MS). Peptides were separated on an Aurora Ultimate column 25cm × 75µm with 1.5 µm media and analyzed on an Orbitrap Ascend Tribrid mass spectrometer (ThermoFisher) coupled to a Vanquish Neo UHPLC (ThermoFisher) using a 55-min gradient (5–35.6% acetonitrile, 0.125% formic acid) at a 400 nL/min flow rate. Data-dependent acquisition was used with a mass range of m/z 400–1600. MS1 resolution was set at 120,000, with 50 ms maximum injection time and a 50% normalized automatic gain control (AGC) target. The top 10 most abundant species with charge states 2–6 were subjected to fragmentation. MS2 was performed with standard AGC, 35% normalized collisional energy (NCE), a 120 ms maximum ion injection time, and a 30 s dynamic exclusion window. Fragment ions were further analyzed using multi-notch SPS-MS3 (ref.[105]) with 45% NCE to quantify TMT reporter ions.

Database searching. Database searching was conducted with the Comet algorithm[106] on Masspike, an in-house search engine described previously[106,107]. Searches used a concatenated target–decoy database comprising proteins from *E. coli* ATCC 25404, *Enterobacteria* phage T1, the SeAvs7 expression plasmid, common contaminants (e.g., keratins, trypsin), and their reversed sequences. Parameters were 25 ppm precursor mass tolerance, 1.0 Da fragment mass tolerance, fully tryptic specificity (K/R) with up to three missed cleavages, and variable Met oxidation (+15.9949 Da). For TMT experiments, TMTpro (+304.2071 Da) on Lys residues and peptide

N termini was set as a static modification. Peptide-spectrum matches were filtered by a target–decoy strategy[107–109] to achieve peptide-level false discovery rate (FDR) <1%, considering XCorr, ΔCn, missed cleavages, peptide length, charge state, and precursor mass accuracy. Short peptides (<7 amino acids) were discarded. Proteins were assembled from identified peptides and controlled to protein-level FDR <1%, and proteins supported by fewer than four unique peptides were discarded.

Proteomics quantification. For TMT-based quantification, peptide abundance was measured by TMT reporter ions. Reporter intensities were extracted using a 0.003 Th window centered on the theoretical m/z, selecting the most intense peak. Isotopic impurities were corrected based on the manufacturer's specifications, and TMT signal-to-noise (S/N) values were used for quantification. Peptides were discarded if the summed S/N across 6 channels of each TMT plex was <60 or if isolation specificity was <50%. Protein abundances were computed by summing peptide S/N values. Protein quantification was normalized to ensure equal SeAvs7 protein loading across all TMT channels. SeAvs7 abundance was quantified using peptides mapping to the N-terminal 596 amino acids, including the TwinStrep tag.

Phage genome sequencing. The genomes of all phages isolated from the City of Palo Alto were sequenced using Tn5 tagmentation and paired-end Illumina sequencing, as previously described[9]. Adapter sequences were trimmed from sequencing reads using CutAdapt with parameters --trim-n -q 20 -m 20 -a CTGTCTCTTATACACATCT -A CTGTCTCTTATACACATCT. Trimmed reads were assembled into contigs with SPAdes[110] using the --careful option. Genes were annotated by Prokka[111], Pharokka[112], Phold[113], or by comparison with a reference genome of a highly similar phage in GenBank. Isolated phages were classified and named according to the rules of the International Committee on the Taxonomy of Viruses (ICTV)[114,115]. The identities of core structural and replicative genes were confirmed based on HHpred[98,116] predictions. Phage phylogenies in Fig. 4e and Supplementary Fig. 18b were generated by concatenating alignments of the large terminases and major capsid proteins. Phage genomes in Supplementary Fig. 18b were visualized using pyGenomeViz.

Phage gene library construction. To construct each library, barcoded plasmids containing phage genes were pooled along with 8–12 uniquely barcoded mNeonGreen clones as internal normalization controls. The amount of each plasmid in the library was adjusted to account for variations in *E. coli* growth rates due to phage gene expression, in order to ensure balanced plasmid levels across the library after growth in *E. coli*. To determine these adjustments, an initial pilot pool of plasmids, mixed in equal volumes, was transformed into *E. coli* NovaBlue(DE3) (Millipore Sigma) containing an empty pACYC184-like vector. These cells were grown for 12 h at 37°C on minimal salt LB agar (10 g/L tryptone, 5 g/L yeast extract, 0.5 g/L NaCl, 7 g/L agar) containing 100 µg/mL carbenicillin, 25 µg/mL chloramphenicol, and 0.005% arabinose. The relative barcode abundances from plasmids isolated from surviving colonies were quantified by deep sequencing. Based on these abundances, the volume of each plasmid added to the final library was adjusted accordingly.

Competent cell production. *E. coli* strains were cultured in ZymoBroth with 25 µg/mL chloramphenicol and made competent using a Mix & Go Transformation Kit (Zymo) according to the manufacturer's recommended protocol.

Co-expression toxicity screens. Co-expression screens for all Avs systems were performed in *E. coli* NovaBlue(DE3), with the exception of Avs21, which was performed in *E. coli* Stbl3 instead due to its toxicity in *E. coli* NovaBlue(DE3). *E. coli* strains containing Avs plasmids were made competent and transformed with 50 ng of the phage gene library, followed by a 30-minute incubation on ice, a 1 minute heat shock at 42 °C, and a 1 h outgrowth at 37°C in SOC (super optimal broth with catabolite repression). Transformed cells were grown on LB agar plates containing 25 µg/mL chloramphenicol, 100 µg/mL carbenicillin, and 0.01% arabinose. Cells expressing Avs2, Avs14, Avs18, and Avs21 were grown on LB agar Lennox (10 g/L tryptone, 5 g/L yeast extract, 5 g/L NaCl, 7 g/L agar), while cells expressing other Avs families were grown on LB agar with minimal salt (10 g/L tryptone, 5 g/L yeast extract, 0.5 g/L NaCl, 7 g/L agar). For each sample, a corresponding empty vector control was grown in parallel using the same strain and media. Plates were incubated for 12 h at 37 °C, and plasmids from surviving colonies were isolated by miniprep (Qiagen). Barcodes were amplified using Q5 polymerase over 8 cycles of PCR with primers containing Illumina sequencing adaptors and sample-specific 8-nt indexes. Purified amplicons were sequenced on a NextSeq 550 (Illumina) with 20 cycles for Read 1. Barcode counts for each plasmid were determined from demultiplexed FASTQ files, requiring a perfect 20 bp match.

For each sample, barcode counts were normalized by dividing them by the average of the mNeonGreen counts within that sample. For each barcode, synthetic toxicity was then quantified as q = (normalized count in Avs sample) / (normalized count in the empty vector (no-Avs) control). For phage genes represented by multiple barcodes, q values were averaged across all barcodes for that gene to obtain a single q value. Fold depletion was calculated as $1/q$.

Anion exchange chromatography. Anion exchange chromatography was performed using an ÄKTA Explorer (Cytiva) equipped with a HiTrap Q HP column (Cytiva). A linear NaCl gradient (0–1 M) in presence of 20 mM Tris-HCl pH 7.5 was applied to purify proteins. Fractions were monitored by UV absorbance at 214, 260, 280 nm and SDS-PAGE. Desired fractions were concentrated using Amicon Ultra centrifugal filters (Millipore).

Size-exclusion chromatography. Size-exclusion chromatography (SEC) was performed using an ÄKTA Explorer (Cytiva) equipped with a Superose 6 10/300 GL column (Cytiva). The column was pre-equilibrated with either an ATP-containing SEC buffer (20 mM Tris-HCl pH 7.5, 0.2 M NaCl,

0.1 mM ATP, and 2 mM $MgCl_2$) or an ATP-free SEC buffer (20 mM Tris-HCl pH 7.5, 0.2 M NaCl). Fractions were monitored by UV absorbance at 214, 260, 280 nm and SDS-PAGE. Desired fractions were concentrated using Amicon Ultra centrifugal filters (Millipore).

Protein purification. Plasmids encoding ZL19 MCP-TwinStrep (TS), TS-SUMO-SeAvs7 variants, TS-EcEF-Tu-His_6, TS-SUMO-MvAvs13, TS-SUMO-PhiV-1 tail nozzle, TS-SUMO-KpAvs20, or TS-SUMO-HdK1 RecA were transformed into *E. coli* Rosetta (DE3) (Fisher Scientific) or BL21 (DE3) (New England Biolabs). Transformed cells were plated on LB agar and incubated overnight at 37 °C. Single colonies were inoculated into Terrific Broth (TB) with 100 µg/mL carbenicillin and grown overnight at 37 °C. Starter cultures were diluted 1:100 into fresh TB and grown at 37 °C to an OD_{600} of 0.8. Protein expression was induced with 0.05–0.1 mM IPTG, and cultures were incubated at 22 °C for 16 h with ~220 rpm orbital shaking. Cells were harvested by centrifugation, and pellets were stored at -80 °C.

To purify proteins other than EcEF-Tu, pellets were resuspended in lysis buffer (50 mM Tris-HCl pH 7.5, 500 mM NaCl, 5% glycerol (v/v), 1 mM DTT, 1 mM ATP, 5 mM $MgCl_2$, 1x cOmplete Protease Inhibitor (Sigma Aldrich)) and lysed using an LM20 Microfluidizer (Microfluidics) at 28,000 PSI. Lysates were clarified by centrifugation at 32,000 ×g for 30 minutes at 4 °C, and the supernatant was incubated with Strep-Tactin Superflow Plus resin (Qiagen) for 1 h at 4 °C. Resin-bound proteins were washed three times with the lysis buffer on a Poly-Prep chromatography column (Bio-Rad). ZL19 MCP was eluted with a buffer containing 20 mM Tris-HCl pH 7.5, 5 mM desthiobiotin. For all other proteins, bdSENP1 protease was added for on-resin cleavage and incubated overnight at 4 °C, and proteins were eluted with 20 mM Tris-HCl pH 7.5. Proteins were further purified by anion exchange chromatography, and buffers were exchanged to 20 mM Tris-HCl pH 7.5, 0.2 M NaCl using Amicon Ultra centrifugal filters (Millipore). For nuclease activity assays, proteins were additionally polished by SEC in ATP-free SEC buffer.

For TS-EcEF-Tu-His_6, pellets were resuspended in His-lysis buffer (50 mM Tris-HCl pH 7.5, 0.3 M NaCl, 40 mM imidazole, 5 % glycerol (v/v), 1x cOmplete protease inhibitor) and lysed by microfluidizer. Clarified lysate was incubated with Ni-NTA Superflow resin (Qiagen), and resin-bound protein was washed three times with His-lysis buffer and eluted with His-elution buffer (50 mM Tris-HCl pH 7.5, 0.1 M NaCl, 500 mM imidazole, 5 % glycerol). The eluates were incubated with Strep-Tactin Superflow Plus resin, which was then washed three times with lysis buffer and eluted with 5 mM desthiobiotin. The protein was further purified by anion exchange chromatography. Final polishing was performed by size-exclusion chromatography using a HiLoad 16/600 Superdex 200 pg column (Cytiva) pre-equilibrated with ATP-free SEC buffer. Protein concentration was determined by UV absorbance at 280 nm.

In vitro DNA cleavage assay. SeAvs7 (0 or 320 nM), ZL19 MCP-TS (0–3.2 µM), and TS-EcEF-Tu-His_6 (0 or 10 µM) were incubated in a reaction buffer containing 20 mM Tris-HCl (pH 7.5), 0.2 M NaCl, 0–1 mM ATP (or ADP or AMP-PNP as specified), and 5 mM $MgCl_2$ for 15 minutes at room temperature. DNA was added at a final concentration of 5 ng/µL, and the reaction mixture was incubated at room temperature for 15 minutes or for the indicated times. DNA products were purified using QIAquick PCR purification columns (Qiagen) and analyzed by gel electrophoresis on an E-Gel EX 2% agarose gel (ThermoFisher).

Complex formation and purification. For SeAvs7 variant:ZL19 MCP complex, SeAvs7 variant (5 µM; 1 eq.) was incubated with ZL19 MCP (10 µM; 2 eq.) and EcEF-Tu (0 or 10 µM; 0 or 2 eq.) in a buffer containing 20 mM Tris-HCl (pH 7.5), 0.2 M NaCl, 1 mM ATP, 5 mM $MgCl_2$, and 1 mM DTT for 1 h at room temperature. For the other Avs:phage trigger pairs, Avs protein (10 µM; 1 eq.) was incubated with the cognate phage protein (10 µM; 2 eq.) in the same buffer for 30 minutes at room temperature. Complexes were purified by SEC using an ATP-containing SEC buffer.

Cryo-EM sample preparation. To assemble the SeAvs7 complex, Strep-Tactin–purified SeAvs7 (5 µM) was incubated with Strep-Tactin–purified ZL19 MCP-TS (10 µM) in 50 mM Tris-HCl (pH 7.5), 0.5 M NaCl, 1 mM ATP, 5 mM $MgCl_2$, 1 mM DTT, and 5% glycerol (v/v) for 1 h at room temperature. The resulting complex was purified by SEC using a Superose 6 10/300 Increase GL column equilibrated with SEC buffer containing 20 mM Tris-HCl (pH 7.5), 0.2 M NaCl, 0.1 mM ATP, and 2 mM $MgCl_2$. For apo SeAvs7, Strep-Tactin–purified SeAvs7 was directly separated by SEC under the same conditions. The ATP-free SEC buffer was also used for comparison in Supplementary Fig. 10b.

Cryo-EM sample preparation and data collection. To prepare cryo-EM grids, 3 µL of EcEF-Tu-bound apo SeAvs7 (5 mg/mL) or the SeAvs7-ZL19 MCP-EcEF-Tu complex (3 mg/mL) was applied to freshly glow-discharged 300-mesh Quantifoil R1.2/1.3 holey carbon grids. The grids were vitrified in liquid ethane using a Vitrobot Mark IV (ThermoFisher) at 4 °C and 100% humidity, with blotting conditions set to a wait time of 5 seconds, a blot time of 3 seconds, and a blot force of 3. Cryo-EM data were collected on a 300 kV Titan Krios (S2C2/Stanford or cEMc/Stanford) equipped with a Falcon 4 detector (ThermoFisher) using EPU software in counting mode. For apo SeAvs7, images were acquired at a nominal magnification of 130,000x, corresponding to a physical pixel size of 0.946 Å. For the SeAvs7-ZL19 MCP-EcEF-Tu complex, images were collected at the same magnification, with a pixel size of 0.95 Å. A total of 40 movie stacks per sample were recorded, each with a total electron dose of 50 electrons per $Å^2$.

Cryo-EM data processing. For the SeAvs7:ZL19 MCP:EcEF-Tu complex, 5,805 movies were processed using cryoSPARC live v4.4, including Patch motion correction, Patch CTF estimation, template picking, and particle extraction with a box of 120 pixels and 4×4 binning. A total of 5,704 images with a CTF resolution better than 8 Å were

selected, resulting in 3,769,341 particles. After two rounds of 2D classification, 487,281 particles were selected for ab initio reconstruction to generate initial models. Following two rounds of heterogeneous refinement, 312,068 particles (in two groups containing 205,105 and 106,963 particles) were re-extracted with a box size of 480 pixels. The 205,105 particles in the first group were subjected to one additional round of heterogeneous refinement, after which 78,090 particles were selected for non-uniform refinement, yielding a 3.43 Å resolution map of the tetrameric complex (Map A). To improve the resolution of the four SeAvs7 TPR:ZL19 MCP:EcEF-Tu interfaces, local refinement was performed individually, yielding improved resolutions of 4.01 Å (Map B), 3.78 Å (Map C), 3.77 Å (Map D), and 3.70 Å (Map E), respectively. A composite map (Map F) was generated by combining Maps A–F in Phenix. As SeAvs7 TPR:ZL19 MCP:EcEF-Tu domains were structurally similar, all particles were aligned using the volume alignment tool, resulting in 312,068 particles subjected to further 3D classification, yielding 59,867 particles. These domains were consistent with those of the SeAvs7:ZL19 MCP:EcEF-Tu monomeric complex from the second particle group (with 106,963 particles). Therefore, these particles were combined with the second particle group, resulting in a total of 166,830 particles. These underwent additional 3D classification and local refinement, producing a final 3.40 Å map (Map G). Maps A-E were sharpened by Local resolution filter, and local resolution was estimated using BlocRes.

For the apo SeAvs7 dataset, 1,209 movies were initially motion corrected using MotionCorr2 (ref.[117]). The dose-weighted images were imported into cryoSPARC v4.4 (ref.[118]), where the contrast transfer function (CTF) was estimated using Patch CTF estimation. Template-based particle picking identified 800,233 particles with a box size of 80 pixels and 4×4 binning. After one round of 2D classification, 304,831 particles were selected for ab initio reconstruction, yielding three initial models for subsequent heterogeneous refinement. The entire set of 800,233 particles was subjected to two rounds of heterogeneous refinement, resulting in 207,066 particles. This subset was re-extracted with a box of 320 pixels and further refined using non-uniform refinement, producing a final map at 2.72 Å resolution. Local resolution was estimated using BlocRes, and the map was sharpened using Local resolution filter.

Model building and refinement. Initial models for all structures were generated using AlphaFold3 predictions and subsequently fitted into the cryo-EM map using Chimera. Iterative manual model building was performed using Coot[119]. The adjusted models were then refined using Phenix[120] to optimize geometry and stereochemistry. Additionally, refinement was performed using e2gmm_model_refine.py[121] in EMAN2 (ref.[122]) to achieve improved PDB validation scores. Model quality was assessed by MolProbity. Structures were visualized using PyMOL (Schrödinger) and ChimeraX[123].

Structural analyses. Structural models for proteins and complexes were generated with AlphaFold3 or with AlphaFold multimer in ColabFold[124], requiring a minimum interface predicted template modeling (ipTM) score of 0.7 for Avs complexes. Structures were visualized with PyMOL (Schrödinger) or ChimeraX 1.8 (UCSF). Structure-guided alignments of homologous phage target proteins were obtained with PROMALS3D[57], using AlphaFold3 models as inputs. Alignable regions, corresponding to the core folds of the target proteins, were used to determine pairwise sequence identity.

To assess the generalizability of Avs7:MCP:EF-Tu complex formation across Avs7 homologs, structures were predicted as a five-component complex (one each of XxAvs7, XxEF-Tu, ZL19 MCP, ATP, and Mg^{2+}, where Xx represents distinct bacterial species), with AlphaFold3. Structures were clustered along with the cryo-EM structure of the SeAvs7:ZL19 MCP:EcEF-Tu monomeric complex using Foldseek multimer-cluster at 60% coverage and a TM-score of 0.70 (Supplementary Table 12)[125]. Structures that clustered with the cryo-EM reference are shown in Supplementary Fig. 17d.

ACKNOWLEDGEMENTS

We thank Dennis Black and Bill Li for assistance with wastewater sample collection, Bharti Singal at Stanford cEMc for assistance with EM data collection, Ross Tomaino for mass spectrometry analysis (Taplin Biological Mass Spectrometry Facility, Harvard Medical School), and Gao lab members for discussions. Some of this work was performed at the Stanford-SLAC Cryo-EM Center (S2C2), which is supported by the National Institutes of Health Common Fund Transformative High-Resolution Cryo-Electron Microscopy program (U24 GM129541). K.S.M., Y.I.W, and E.V.K. are supported by intramural funds of the U.S. Department of Health and Human Services (to National Library of Medicine). C.C. is supported by a training grant from NIH Cellular and Molecular Training Grant (NIGMS, grant number 5T32GM007276). S.A.E. is supported by an NIH Genetics and Developmental Biology Training Grant (NIGMS, grant number 5T32GM141828) and by Stanford Bio-X. H.X. is supported by NIH R00AG07346103, the Shmunis Family Innovation Award in Cancer Therapeutics, the Baxter Foundation Faculty Scholars Award, and the V Scholar Award. L.F. is supported by the G. Harold and Leila Y. Mathers Foundation and NIH R35GM153424. A.G. is supported by the G. Harold & Leila Y. Mathers Foundation, the Esther Ehrman Lazard Faculty Scholars Program, and Stanford Bio-X.

AUTHOR CONTRIBUTIONS

H.L. and A.G. conducted bioinformatic analyses of Avs7/Dsr1 and generated AlphaFold models. K.S.M., Y.I.W., E.V.K., H.L., and A.G. performed bioinformatics analyses of STAND NTPases. H.L. performed biochemical experiments, analyzed structures, and generated structural figures. H.L. and A.G. isolated and sequenced phages from wastewater. S.L.-W. and A.G. cloned Avs genes, created phage gene libraries, and performed co-expression toxicity experiments. S.L.-W., C.C., H.L., and A.G. performed phage plaque assays. H.L., S.L.-W., S.A.E., and C.C. purified proteins. J.Z. prepared grids and performed cryo-EM data collection, structure determination, and model building. J.C. and H.X. performed mass spectrometry of SeAvs7 pulldowns. L.F. oversaw cryo-EM studies. All authors analyzed data. A.G. conceived the project and supervised research. H.L., S.L.-W., C.C., and A.G. wrote the manuscript with input from all authors.

COMPETING INTERESTS

The authors declare no competing interests.

DATA AVAILABILITY

Cryo-EM maps have been deposited in the Electron Microscopy Data Bank under accession numbers EMD-73001 (Map F; Composite map of SeAvs7:ZL19 MCP:EcEF-Tu tetrameric complex), EMD-73002 (Map B), EMD-73003 (Map A), EMD-73004 (Map E), EMD-73005 (Map D), EMD-73006 (Map C), and EMD-48771 (Apo SeAvs7) and EMD-48772 (Map G; SeAvs7:ZL19 MCP:EcEF-Tu monomeric complex). The corresponding atomic models have been deposited in the Protein Data Bank under accession codes 9YIX (Map F), 9N01 (Map G) and 9N00 (Apo SeAvs7).

References

1. Koonin, E. V. & Aravind, L. Origin and evolution of eukaryotic apoptosis: the bacterial connection. *Cell Death Differ* **9**, 394–404 (2002).

2. Leipe, D. D., Koonin, E. V. & Aravind, L. STAND, a class of P-loop NTPases including animal and plant regulators of programmed cell death: multiple, complex domain architectures, unusual phyletic patterns, and evolution by horizontal gene transfer. *J Mol Biol* **343**, 1–28 (2004).

3. Jones, J. D. G., Vance, R. E. & Dangl, J. L. Intracellular innate immune surveillance devices in plants and animals. *Science* **354**, (2016).

4. Zhao, Y. et al. The NLRC4 inflammasome receptors for bacterial flagellin and type III secretion apparatus. *Nature* **477**, 596–600 (2011).

5. Kofoed, E. M. & Vance, R. E. Innate immune recognition of bacterial ligands by NAIPs determines inflammasome specificity. *Nature* **477**, 592–595 (2011).

6. Chamaillard, M. et al. An essential role for NOD1 in host recognition of bacterial peptidoglycan containing diaminopimelic acid. *Nat Immunol* **4**, 702–707 (2003).

7. Girardin, S. E. et al. Nod2 is a general sensor of peptidoglycan through muramyl dipeptide (MDP) detection. *J Biol Chem* **278**, 8869–8872 (2003).

8. Narumi, S. et al. SAMD9 mutations cause a novel multisystem disorder, MIRAGE syndrome, and are associated with loss of chromosome 7. *Nat Genet* **48**, 792–797 (2016).

9. Gao, L. et al. Diverse enzymatic activities mediate antiviral immunity in prokaryotes. *Science* **369**, 1077–1084 (2020).

10. Gao, L. A. et al. Prokaryotic innate immunity through pattern recognition of conserved viral proteins. *Science* **377**, eabm4096 (2022).

11. Béchon, N. et al. Diversification of molecular pattern recognition in bacterial NLR-like proteins. *Nat Commun* **15**, 9860 (2024).

12. Conte, A. N. et al. DnaJ mediates phage sensing by the bacterial NLR-related protein bNACHT25. *PLoS Biol* **23**, e3003203 (2025).

13. Vassallo, C. N., Doering, C. R., Littlehale, M. L., Teodoro, G. I. C. & Laub, M. T. A functional selection reveals previously undetected anti-phage defence systems in the *E. coli* pangenome. *Nat Microbiol* **7**, 1568–1579 (2022).

14. Rousset, F. et al. Phages and their satellites encode hotspots of antiviral systems. *Cell Host Microbe* **30**, 740–753.e5 (2022).

15. Kibby, E. M. et al. Bacterial NLR-related proteins protect against phage. *Cell* **186**, 2410–2424.e18 (2023).

16. van den Berg, D. F. et al. Bacterial homologs of innate eukaryotic antiviral defenses with anti-phage activity highlight shared evolutionary roots of viral defenses. *Cell Host Microbe* **32**, 1427–1443.e8 (2024).

17. Legrand, A. et al. Evolutionary characterization of antiviral SAMD9/9L across kingdoms supports ancient convergence and lineage-specific adaptations. *Nat Ecol Evol* **9**, 2206–2222 (2025).

18. Neuwald, A. F., Aravind, L., Spouge, J. L. & Koonin, E. V. AAA+: A class of chaperone-like ATPases associated with the assembly, operation, and disassembly of protein complexes. *Genome Res* **9**, 27–43 (1999).

19. Rousset, F. et al. A conserved family of immune effectors cleaves cellular ATP upon viral infection. *Cell* **186**, 3619–3631.e13 (2023).

20. Makarova, K. S., Wolf, Y. I., Snir, S. & Koonin, E. V. Defense islands in bacterial and archaeal genomes and prediction of novel defense systems. *J Bacteriol* **193**, 6039–6056 (2011).

21. Doron, S. et al. Systematic discovery of antiphage defense systems in the microbial pangenome. *Science* **359**, (2018).

22. Shmakov, S. A., Makarova, K. S., Wolf, Y. I., Severinov, K. V. & Koonin, E. V. Systematic prediction of genes functionally linked to CRISPR-Cas systems by gene neighborhood analysis. *Proc Natl Acad Sci* **115**, E5307–E5316 (2018).

23. Brenes, L. R. & Laub, M. T. *E. coli* prophages encode an arsenal of defense systems to protect against temperate phages. *Cell Host Microbe* **33**, 1004–1018.e5 (2025).

24. Chou, W.-C., Jha, S., Linhoff, M. W. & Ting, J. P.-Y. The NLR gene family: from discovery to present day. *Nat Rev Immunol* **23**, 635–654 (2023).

25. Hu, Z. et al. Structural and biochemical basis for induced self-propagation of NLRC4. *Science* **350**, 399–404 (2015).

26. Zhang, L. et al. Cryo-EM structure of the activated NAIP2-NLRC4 inflammasome reveals nucleated polymerization. *Science* **350**, 404–409 (2015).

27. Xiao, L., Magupalli, V. G. & Wu, H. Cryo-EM structures of the active NLRP3 inflammasome disc. *Nature* **613**, 595–600 (2023).

28. Zhou, M. et al. Atomic structure of the apoptosome: mechanism of cytochrome c- and dATP-mediated activation of Apaf-1. *Genes Dev* **29**, 2349–2361 (2015).

29. Wang, J. et al. Reconstitution and structure of a plant NLR resistosome conferring immunity. *Science* **364**, (2019).

30. Liu, F. et al. Activation of the helper NRC4 immune receptor forms a hexameric resistosome. *Cell* **187**, 4877–4889.e15 (2024).

31. Wu, Y., Sun, Y., Richet, E., Han, Z. & Chai, J. Structural basis for negative regulation of the *Escherichia coli* maltose system. *Nat Commun* **14**, 4925 (2023).

32. Poon, K. K., Chu, J. C. & Wong, S. L. Roles of glucitol in

the GutR-mediated transcription activation process in *Bacillus subtilis*: glucitol induces GutR to change its conformation and to bind ATP. *J Biol Chem* **276**, 29819–29825 (2001).

33. Shi, J. et al. Structural insights into transcription activation of the antibiotic regulatory protein, AfsR. *iScience* **27**, 110421 (2024).

34. Wang, Y. et al. Structural and functional characterization of AfsR, an SARP family transcriptional activator of antibiotic biosynthesis in Streptomyces. *PLoS Biol* **22**, e3002528 (2024).

35. Koonin, E. V. & Aravind, L. The NACHT family - a new group of predicted NTPases implicated in apoptosis and MHC transcription activation. *Trends Biochem Sci* **25**, 223–224 (2000).

36. Mekhedov, S. L., Makarova, K. S. & Koonin, E. V. The complex domain architecture of SAMD9 family proteins, predicted STAND-like NTPases, suggests new links to inflammation and apoptosis. *Biol Direct* **12**, 13 (2017).

37. Dierks, T. et al. Molecular basis for multiple sulfatase deficiency and mechanism for formylglycine generation of the human formylglycine-generating enzyme. *Cell* **121**, 541–552 (2005).

38. Kaur, G., Burroughs, A. M., Iyer, L. M. & Aravind, L. Highly regulated, diversifying NTP-dependent biological conflict systems with implications for the emergence of multicellularity. *Elife* **9**, (2020).

39. Furano, A. V. Content of elongation factor Tu in *Escherichia coli*. *Proc Natl Acad Sci* **72**, 4780–4784 (1975).

40. Fu, J., Schroder, K. & Wu, H. Mechanistic insights from inflammasome structures. *Nat Rev Immunol* **24**, 518–535 (2024).

41. Suhanovsky, M. M. & Teschke, C. M. Nature's favorite building block: Deciphering folding and capsid assembly of proteins with the HK97-fold. *Virology* **479-480**, 487–497 (2015).

42. Duda, R. L. & Teschke, C. M. The amazing HK97 fold: versatile results of modest differences. *Curr Opin Virol* **36**, 9–16 (2019).

43. Koonin, E. V. et al. Global organization and proposed megataxonomy of the virus world. *Microbiol Mol Biol Rev* **84**, (2020).

44. Helgstrand, C. et al. The refined structure of a protein catenane: the HK97 bacteriophage capsid at 3.44 Å resolution. *J Mol Biol* **334**, 885–899 (2003).

45. Hryc, C. F. et al. Accurate model annotation of a near-atomic resolution cryo-EM map. *Proc Natl Acad Sci* **114**, 3103–3108 (2017).

46. Abramson, J. et al. Accurate structure prediction of biomolecular interactions with AlphaFold 3. *Nature* **630**, 493–500 (2024).

47. Johansen, J. S. et al. *E. coli* elongation factor Tu bound to a GTP analogue displays an open conformation equivalent to the GDP-bound form. *Nucleic Acids Res* **46**, 8641–8650 (2018).

48. Loveland, A. B., Demo, G. & Korostelev, A. A. Cryo-EM of elongating ribosome with EF-Tu•GTP elucidates tRNA proofreading. *Nature* **584**, 640–645 (2020).

49. Song, H., Parsons, M. R., Rowsell, S., Leonard, G. & Phillips, S. E. Crystal structure of intact elongation factor EF-Tu from *Escherichia coli* in GDP conformation at 2.05 Å resolution. *J Mol Biol* **285**, 1245–1256 (1999).

50. Dion, M. B., Oechslin, F. & Moineau, S. Phage diversity, genomics and phylogeny. *Nat Rev Microbiol* **18**, 125–138 (2020).

51. Veesler, D. & Cambillau, C. A common evolutionary origin for tailed-bacteriophage functional modules and bacterial machineries. *Microbiol Mol Biol Rev* **75**, 423–33, first page of table of contents (2011).

52. Nagy, T. A., Gersabeck, G. W., Conte, A. N. & Whiteley, A. T. Identifying phage proteins that activate the bacterial innate immune system. *bioRxiv* (2025) doi:10.1101/2025.07.02.662641.

53. Czernecki, D., Nourisson, A., Legrand, P. & Delarue, M. Reclassification of family A DNA polymerases reveals novel functional subfamilies and distinctive structural features. *Nucleic Acids Res* **51**, 4488–4507 (2023).

54. Iyer, L. M., Koonin, E. V. & Aravind, L. Classification and evolutionary history of the single-strand annealing proteins, RecT, Redβ, ERF and RAD52. *BMC Genomics* **3**, 8 (2002).

55. Zinke, M., Schröder, G. F. & Lange, A. Major tail proteins of bacteriophages of the order *Caudovirales*. *J Biol Chem* **298**, 101472 (2022).

56. Xu, J., Hendrix, R. W. & Duda, R. L. Chaperone-protein interactions that mediate assembly of the bacteriophage lambda tail to the correct length. *J Mol Biol* **426**, 1004–1018 (2014).

57. Pei, J., Kim, B.-H. & Grishin, N. V. PROMALS3D: a tool for multiple protein sequence and structure alignments. *Nucleic Acids Res* **36**, 2295–2300 (2008).

58. Leipe, D. D., Aravind, L., Grishin, N. V. & Koonin, E. V. The bacterial replicative helicase DnaB evolved from a RecA duplication. *Genome Res* **10**, 5–16 (2000).

59. Georgiou, T. et al. Specific peptide-activated proteolytic cleavage of *Escherichia coli* elongation factor Tu. *Proc Natl Acad Sci* **95**, 2891–2895 (1998).

60. Zhang, T. et al. Direct activation of a bacterial innate immune system by a viral capsid protein. *Nature* **612**, 132–140 (2022).

61. Garb, J. et al. Multiple phage resistance systems inhibit infection via SIR2-dependent NAD depletion. *Nat Microbiol* **7**, 1849–1856 (2022).

62. Huang, J. et al. Molecular basis of bacterial DSR2 anti-phage defense and viral immune evasion. *Nat Commun* **15**, 3954 (2024).

63. Wang, R. et al. The structural basis of the activation and inhibition of DSR2 NADase by phage proteins. *Nat Commun* **15**, 6185 (2024).

64. Zhang, H. et al. Structural insights into activation mechanisms on NADase of the bacterial DSR2 anti-phage defense system. *Sci Adv* **10**, eadn5691 (2024).

65. Stokar-Avihail, A. et al. Discovery of phage determinants that confer sensitivity to bacterial immune systems. *Cell* **186**, 1863–1876.e16 (2023).

66. Ackermann, H.-W. 5500 Phages examined in the electron microscope. *Arch Virol* **152**, 227–243 (2007).

67. Kao, C., Gumbs, E. & Snyder, L. Cloning and characterization of the Escherichia coli lit gene, which blocks bacteriophage T4 late gene expression. *J Bacteriol* **169**, 1232–1238 (1987).

68. Bergsland, K. J., Kao, C., Yu, Y. T., Gulati, R. & Snyder, L. A site in the T4 bacteriophage major head protein gene that can promote the inhibition of all translation in *Escherichia coli*. *J Mol Biol* **213**, 477–494 (1990).

69. Zhang, T. et al. A bacterial immunity protein directly senses two disparate phage proteins. *Nature* **635**, 728–735 (2024).

70. Bouchard, J. D. & Moineau, S. Lactococcal phage genes involved in sensitivity to AbiK and their relation to single-strand annealing proteins. *J Bacteriol* **186**, 3649–3652 (2004).

71. Yasui, R., Washizaki, A., Furihata, Y., Yonesaki, T. & Otsuka, Y. AbpA and AbpB provide anti-phage activity in *Escherichia coli*. *Genes Genet Syst* **89**, 51–60 (2014).

72. Depardieu, F. et al. A eukaryotic-like serine/threonine kinase protects Staphylococci against phages. *Cell Host Microbe* **20**, 471–481 (2016).

73. Yu, Y. T. & Snyder, L. Translation elongation factor Tu cleaved by a phage-exclusion system. *Proc Natl Acad Sci* **91**, 802–806 (1994).

74. Bingham, R., Ekunwe, S. I., Falk, S., Snyder, L. & Kleanthous, C. The major head protein of bacteriophage T4 binds specifically to elongation factor Tu. *J Biol Chem* **275**, 23219–23226 (2000).

75. Rousset, F. et al. TIR signaling activates caspase-like immunity in bacteria. *Science* **387**, 510–516 (2025).

76. Schmitz, M., Querques, I., Oberli, S., Chanez, C. & Jinek, M. Structural basis for the assembly of the type V CRISPR-associated transposon complex. *Cell* **185**, 4999–5010.e17 (2022).

77. Kidmose, R. T., Vasiliev, N. N., Chetverin, A. B., Andersen, G. R. & Knudsen, C. R. Structure of the Qβ replicase, an RNA-dependent RNA polymerase consisting of viral and host proteins. *Proc Natl Acad Sci* **107**, 10884–10889 (2010).

78. Takeshita, D. & Tomita, K. Assembly of Qβ viral RNA polymerase with host translational elongation factors EF-Tu and -Ts. *Proc Natl Acad Sci* **107**, 15733–15738 (2010).

79. Harvey, K. L., Jarocki, V. M., Charles, I. G. & Djordjevic, S. P. The diverse functional roles of elongation factor Tu (EF-Tu) in microbial pathogenesis. *Front Microbiol* **10**, 2351 (2019).

80. Sharif, H. et al. Structural mechanism for NEK7-licensed activation of NLRP3 inflammasome. *Nature* **570**, 338–343 (2019).

81. Schäffer, A. A. et al. Improving the accuracy of PSI-BLAST protein database searches with composition-based statistics and other refinements. *Nucleic Acids Res* **29**, 2994–3005 (2001).

82. Steinegger, M. & Söding, J. MMseqs2 enables sensitive protein sequence searching for the analysis of massive data sets. *Nat Biotechnol* **35**, 1026–1028 (2017).

83. Edgar, R. C. Muscle5: High-accuracy alignment ensembles enable unbiased assessments of sequence homology and phylogeny. *Nat Commun* **13**, 6968 (2022).

84. Esterman, E. S., Wolf, Y. I., Kogay, R., Koonin, E. V. & Zhaxybayeva, O. Evolution of DNA packaging in gene transfer agents. *Virus Evol* **7**, veab015 (2021).

85. Deorowicz, S., Debudaj-Grabysz, A. & Gudyś, A. FAMSA: Fast and accurate multiple sequence alignment of huge protein families. *Sci Rep* **6**, 33964 (2016).

86. Lefort, V., Desper, R. & Gascuel, O. FastME 2.0: A comprehensive, accurate, and fast distance-based phylogeny inference program. *Mol Biol Evol* **32**, 2798–2800 (2015).

87. Marchler-Bauer, A. et al. CDD/SPARCLE: functional classification of proteins via subfamily domain architectures. *Nucleic Acids Res* **45**, D200–D203 (2017).

88. Yu, G., Smith, D. K., Zhu, H., Guan, Y. & Lam, T. T.-Y. GGTREE: An R package for visualization and annotation of phylogenetic trees with their covariates and other associated data. *Methods Ecol Evol* **8**, 28–36 (2017).

89. Tesson, F. et al. Systematic and quantitative view of the antiviral arsenal of prokaryotes. *Nat Commun* **13**, 2561 (2022).

90. Jumper, J. et al. Highly accurate protein structure prediction with AlphaFold. *Nature* **596**, 583–589 (2021).

91. Varadi, M. et al. AlphaFold Protein Structure Database in 2024: providing structure coverage for over 214 million protein sequences. *Nucleic Acids Res* **52**, D368–D375 (2024).

92. van Kempen, M. et al. Fast and accurate protein structure search with Foldseek. *Nat Biotechnol* **42**, 243–246 (2023).

93. Wishart, D. S. et al. PHASTEST: faster than PHASTER, better than PHAST. *Nucleic Acids Res* **51**, W443–W450 (2023).

94. Altschul, S. F. et al. Gapped BLAST and PSI-BLAST: a new generation of protein database search programs. *Nucleic Acids Res* **25**, 3389–3402 (1997).

95. Katoh, K., Misawa, K., Kuma, K.-I. & Miyata, T. MAFFT: a novel method for rapid multiple sequence alignment based on fast Fourier transform. *Nucleic Acids Res* **30**, 3059–3066 (2002).

96. Capella-Gutiérrez, S., Silla-Martínez, J. M. & Gabaldón, T. trimAl: a tool for automated alignment trimming in large-scale phylogenetic analyses. *Bioinformatics* **25**, 1972–1973 (2009).

97. Nguyen, L.-T., Schmidt, H. A., von Haeseler, A. & Minh, B. Q. IQ-TREE: a fast and effective stochastic algorithm for estimating maximum-likelihood phylogenies. *Mol Biol Evol* **32**, 268–274 (2015).

98. Zimmermann, L. et al. A completely reimplemented MPI Bioinformatics Toolkit with a new HHpred Server at its core. *J Mol Biol* **430**, 2237–2243 (2018).

99. Letunic, I. & Bork, P. Interactive Tree Of Life (iTOL) v5: an online tool for phylogenetic tree display and annotation. *Nucleic Acids Res* **49**, W293–W296 (2021).

100. Minh, B. Q. et al. IQ-TREE 2: New models and efficient methods for phylogenetic inference in the genomic era. *Mol Biol Evol* **37**, 1530–1534 (2020).

101. Steinegger, M. et al. HH-suite3 for fast remote homology detection and deep protein annotation. *BMC Bioinformatics* **20**, 473 (2019).

102. Picelli, S. et al. Tn5 transposase and tagmentation procedures for massively scaled sequencing projects. *Genome Res* **24**, 2033–2040 (2014).

103. Baba, T. et al. Construction of *Escherichia coli* K-12 in-frame, single-gene knockout mutants: the Keio collection. *Mol Syst Biol* **2**, 2006.0008 (2006).

104. Li, J. et al. TMTpro reagents: a set of isobaric labeling mass tags enables simultaneous proteome-wide measurements across 16 samples. *Nat Methods* **17**, 399–404 (2020).

105. McAlister, G. C. et al. MultiNotch MS3 enables accurate, sensitive, and multiplexed detection of differential expression across cancer cell line proteomes. *Anal Chem* **86**, 7150–7158 (2014).

106. Eng, J. K., Jahan, T. A. & Hoopmann, M. R. Comet: an open-source MS/MS sequence database search tool. *Proteomics* **13**, 22–24 (2013).

107. Huttlin, E. L. et al. A tissue-specific atlas of mouse protein phosphorylation and expression. *Cell* **143**, 1174–1189 (2010).

108. Elias, J. E. & Gygi, S. P. Target-decoy search strategy for increased confidence in large-scale protein identifications by mass spectrometry. *Nat Methods* **4**, 207–214 (2007).

109. Peng, J., Elias, J. E., Thoreen, C. C., Licklider, L. J. & Gygi, S. P. Evaluation of multidimensional chromatography coupled with tandem mass spectrometry (LC/LC-MS/MS) for large-scale protein analysis: the yeast proteome. *J Proteome Res* **2**, 43–50 (2003).

110. Bankevich, A. et al. SPAdes: a new genome assembly algorithm and its applications to single-cell sequencing. *J Comput Biol* **19**, 455–477 (2012).

111. Seemann, T. Prokka: rapid prokaryotic genome annotation. *Bioinformatics* **30**, 2068–2069 (2014).

112. Bouras, G. et al. Pharokka: a fast scalable bacteriophage annotation tool. *Bioinformatics* **39**, btac776 (2023).

113. Bouras, G. et al. Protein structure informed bacteriophage genome annotation with phold. *bioRxiv* (2025) doi:10.1101/2025.08.05.668817.

114. Grigson, S. R., Giles, S. K., Edwards, R. A. & Papudeshi, B. Knowing and naming: phage annotation and nomenclature for phage therapy. *Clin Infect Dis* **77**, S352–S359 (2023).

115. Adriaenssens, E. & Brister, J. R. How to name and classify your phage: an informal guide. *Viruses* **9**, (2017).

116. Söding, J., Biegert, A. & Lupas, A. N. The HHpred interactive server for protein homology detection and structure prediction. *Nucleic Acids Res* **33**, W244–8 (2005).

117. Zheng, S. Q. et al. MotionCor2: anisotropic correction of beam-induced motion for improved cryo-electron microscopy. *Nat Methods* **14**, 331–332 (2017).

118. Punjani, A., Rubinstein, J. L., Fleet, D. J. & Brubaker, M. A. cryoSPARC: algorithms for rapid unsupervised cryo-EM structure determination. *Nat Methods* **14**, 290–296 (2017).

119. Emsley, P. & Cowtan, K. Coot: model-building tools for molecular graphics. *Acta Crystallogr D Biol Crystallogr* **60**, 2126–2132 (2004).

120. Adams, P. D. et al. PHENIX: a comprehensive Python-based system for macromolecular structure solution. *Acta Crystallogr D Biol Crystallogr* **66**, 213–221 (2010).

121. Chen, M. Building molecular model series from heterogeneous CryoEM structures using Gaussian mixture models and deep neural networks. *Commun Biol* **8**, 798 (2025).

122. Tang, G. et al. EMAN2: an extensible image processing suite for electron microscopy. *J Struct Biol* **157**, 38–46 (2007).

123. Pettersen, E. F. et al. UCSF ChimeraX: Structure visualization for researchers, educators, and developers. *Protein Sci* **30**, 70–82 (2021).

124. Mirdita, M. et al. ColabFold: making protein folding accessible to all. *Nat Methods* **19**, 679–682 (2022).

125. Kim, W. et al. Rapid and sensitive protein complex alignment with Foldseek-Multimer. *Nat Methods* **22**, 469–472 (2025).

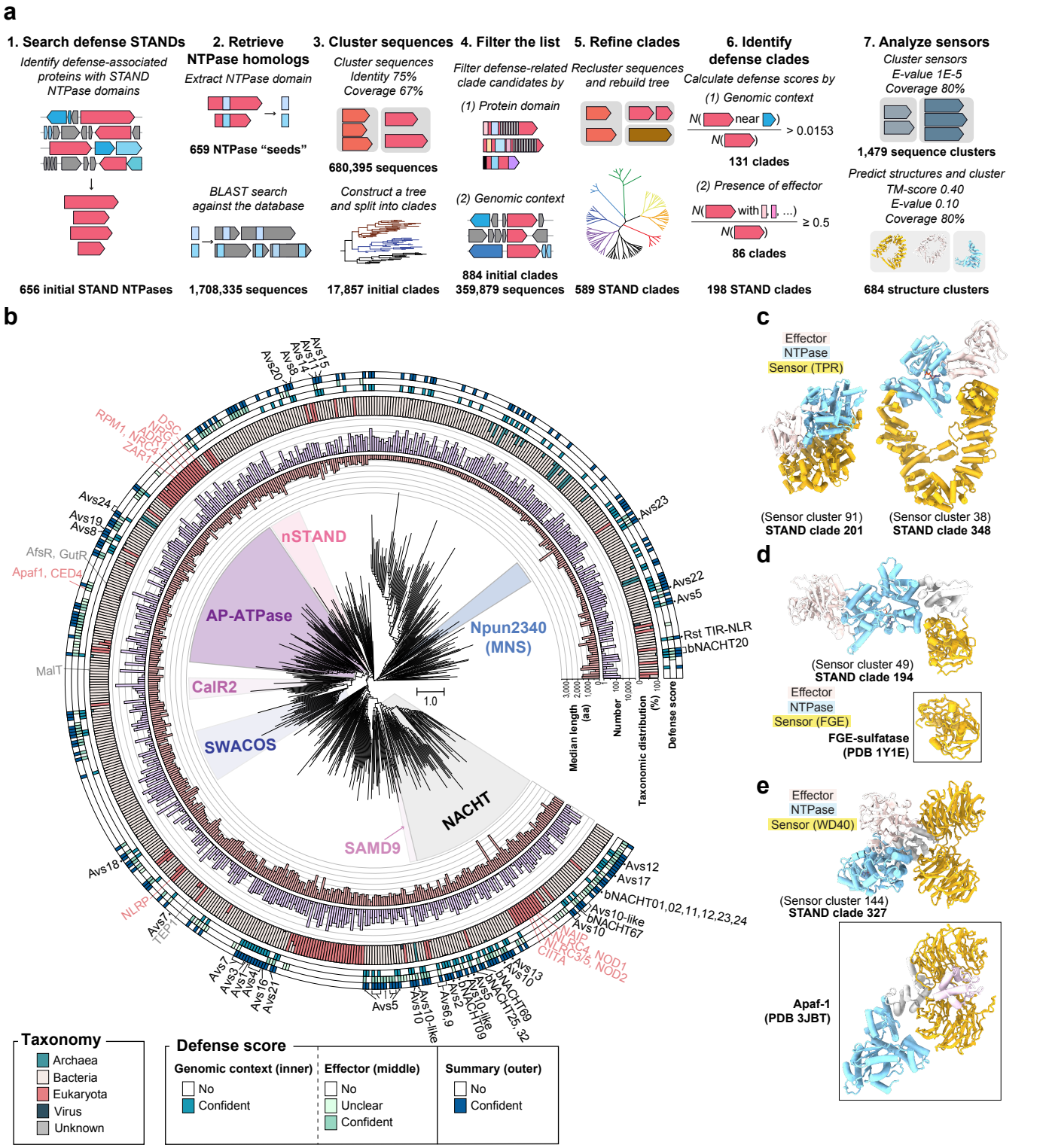

Phylogeny of defense-associated STAND NTPases in prokaryotes. a, Schematic of the workflow to identify, analyze, and classify STAND NTPases. **b,** A maximum likelihood tree of the NTPase domains of 589 clades. MNS, NACHT, SWACOS, CalR2, AP-ATPase, and nSTAND refer to previously defined clades. Eukaryotic STANDs names are annotated in light red text. Defense scores were assigned based on two criteria: the frequency of known defense genes in the genomic neighborhood of STAND genes (genomic context) and proportion of STANDs carrying immune-related effector domains (effector; Supplementary Table 3). Clades were classified as confident defense-associated if they satisfied either criterion. **c–e,** Representative AlphaFold3 structural models of representatives with (c) helical bundles, (d) FGE-sulfatase, or (e) Apaf1-like WD40 β-propellers as sensors. Numbers in parentheses represent structural clusters (1–684). DAS, defense-associated sensor; Avs, antiviral STAND; bNACHT, bacterial NACHT; TPR, tetratricopeptide repeat; TEP1, telomerase-associated protein 1; SAMD9, sterile alpha motif domain containing 9; Apaf-1, apoptotic protease activating factor 1; FGE, formylglycine-generating enzyme.

Figure 1

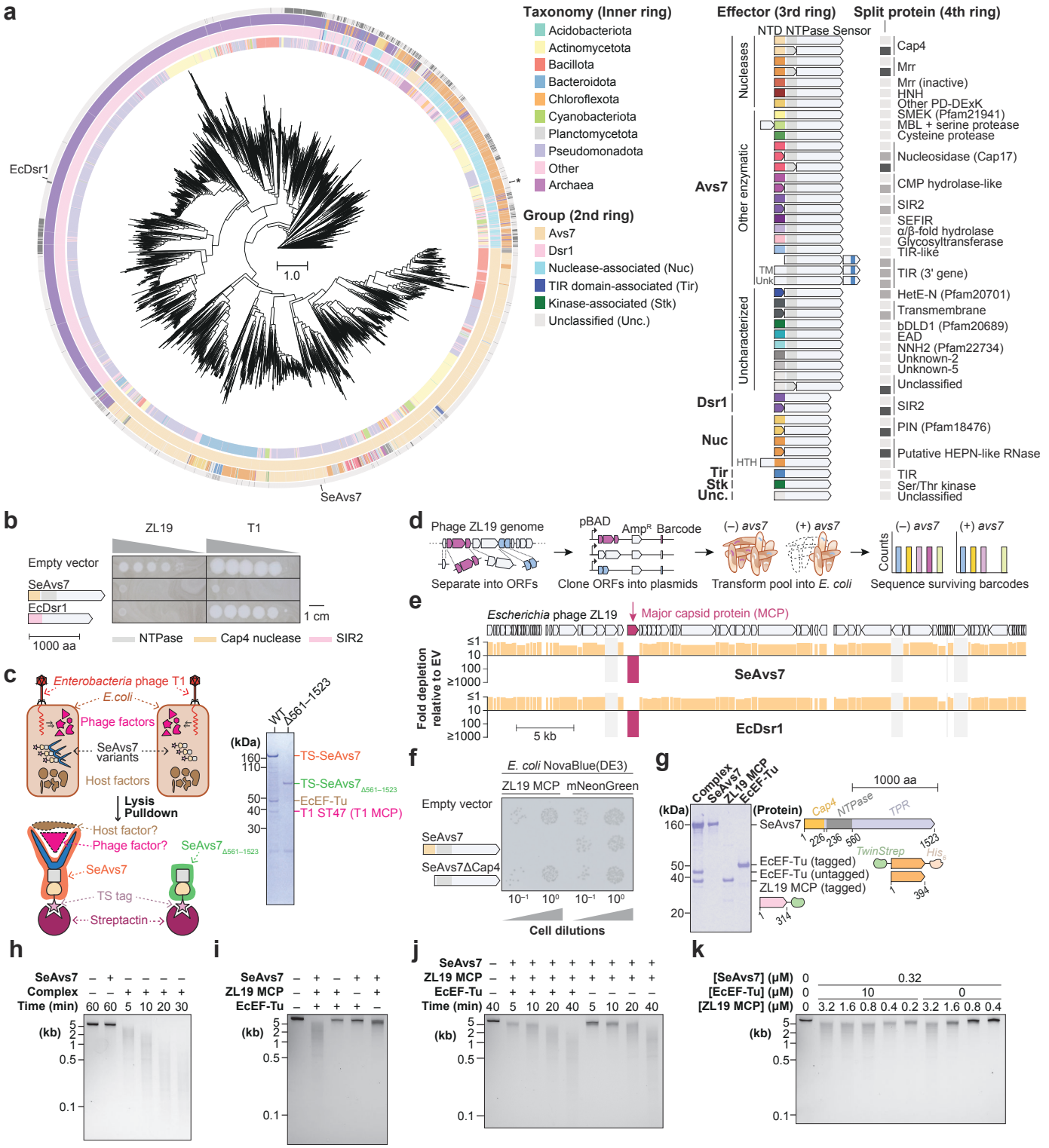

Homologous sensor domains in Avs7 and Dsr1 recognize phage major capsid proteins. a, A maximum likelihood tree of the homologous sensor domains of Avs7, Dsr1, and other anti-phage defense proteins (N = 4,969 representatives). The innermost ri--ng represents taxonomy, and the other three rings together represent the type and domain architecture of the protein. The asteri--sk denotes a HEPN-like RNase-containing protein from *Streptomyces* sp. NBC_00271. Unknown-2 is also fused to several Avs2 homologs (Gao et al. 2022). MBL, metallo-β-lactamase; EAD, effector-associated domain; TM, transmembrane; Unk, unknown. **b,** Plaque assays of *E. coli* with either an empty vector, SeAvs7, or EcDsr1 against *Escherichia* phage ZL19 and *Enterobacteria* phage T1. **c,** A schematic and the SDS-PAGE analysis of the pulldown experiment. **d–e,** A synthetic lethal genetic screen to identify phage triggers that induce SeAvs7- and EcDsr1-mediated cell death. Genes were cloned after an arabinose-inducible pBAD promoter with a unique 20 nt barcode sequence. Amp^R, ampicillin resistance gene. **f,** Photographs of *E. coli* co-transformation assays. **g,** SDS-PAGE analysis of purified recombinant proteins and the oligomeric complex. **h–k,** Agarose gel analysis of the nuclease activity assays using a linear dsDNA substrate in vitro.

Figure 2

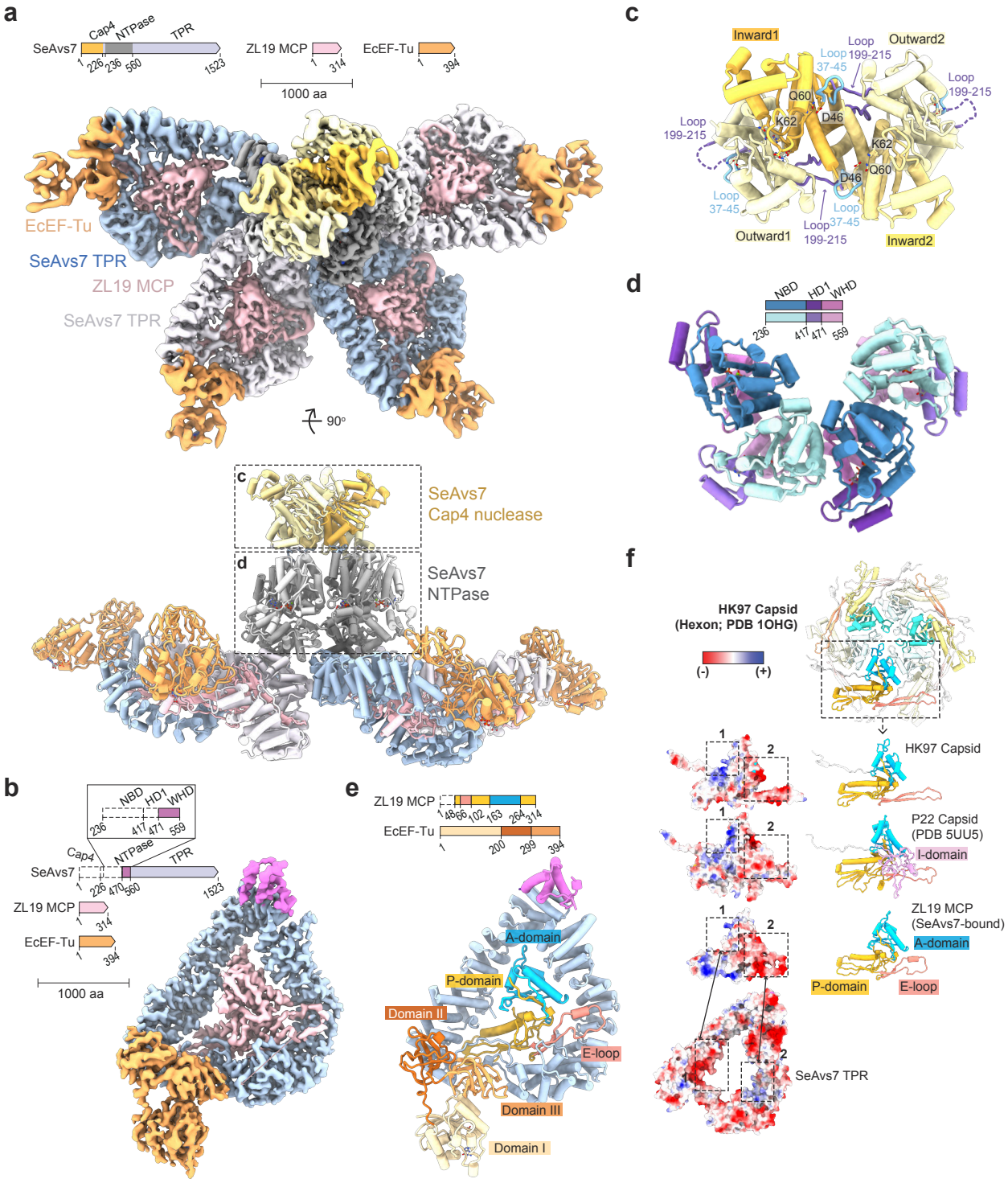

SeAvs7, ZL19 MCP, and EcEF-Tu form an active asymmetric tetramer. a, A composite map (top) and the overall structure of the SeAvs7:ZL19 MCP:EcEF-Tu tetrameric complex. **b**, A cryo-EM map of the SeAvs7:ZL19 MCP:EcEF-Tu monomeric complex. **c–d,** Structure of Cap4 nuclease tetramer (c) and the NTPase tetramer (d). **e,** Overall structure of the SeAvs7:ZL19 MCP:EcEF-Tu monomeric complex. **f**, Structural comparison of the major capsid proteins from diverse tailed dsDNA phages. Electrostatic potent--ial of these capsid proteins and SeAvs7 TPR domain are shown.

Figure 3

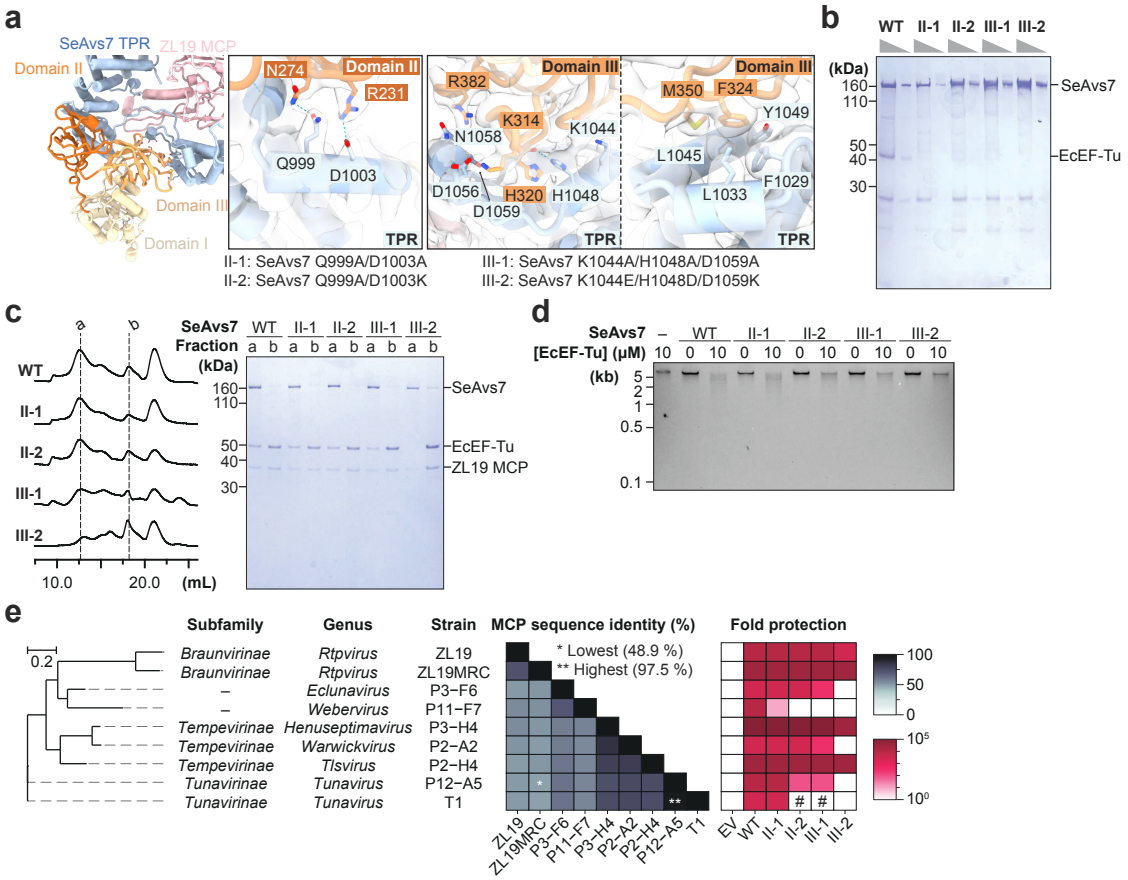

EcEF-Tu enhances the SeAvs7-mediated immune response. a, Interface between SeAvs7 TPR domain and EcEF-Tu domains II-III. Names of the four mutants are shown below (II-1, SeAvs7$^{Q999A/D1003A}$; II-2, SeAvs7$^{Q999A/D1003K}$; III-1, SeAvs7$^{K1044A/H1048A/D1059A}$; III-2, SeAvs7$^{K1044E/H1048D/D1059K}$). **b**, SDS-PAGE analysis of the SeAvs7 wildtype or mutants purified from cell lysate. **c**, Size-exclusion chromatograms of the SeAvs7 variant:ZL19 MCP:EcEF-Tu complex in vitro and SDS-PAGE analysis of the selected fractions. **d**, Agarose gel analysis of the nuclease activity assay. **e**, Phylogeny of the nine *Drexlerviridae* family phages used in this study (left), pairwise sequence identities of the MCPs (middle), and anti-phage activity of proteins against phages (right). # indicates reduced plaque sizes without changing efficiency of plating. EV, empty vector; WT, wildtype.

Figure 4

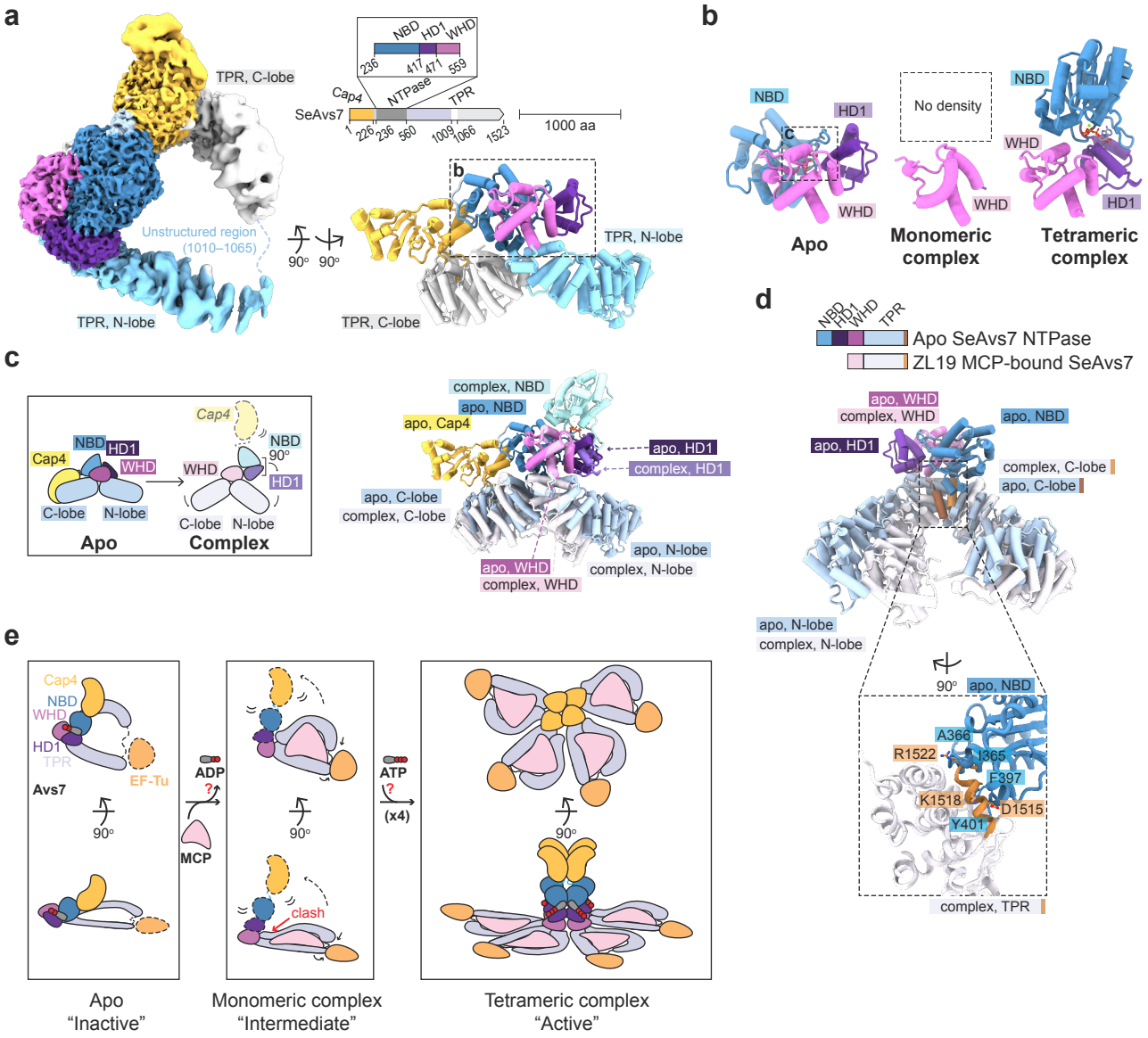

Binding of ZL19 MCP induces structural changes of SeAvs7. a, Cryo-EM map (left) and structure (right) of apo SeAvs7. **b,** Structural comparison of NTPase domains in three different structures. **c,** A structural overlay of apo SeAvs7 and SeAvs7 from a protomer of the tetrameric complex aligned by the WHD. A cartoon depicting the structural change is shown in the left inset. **d,** A modeled SeAvs7 NTPase-TPR bound to both ADP and ZL19 MCP by overlaying apo SeAvs7 and an SeAvs7 protomer of the tetrameric complex by WHD domain. Observed steric clash is shown in the inset. **e,** A proposed mechanism of ZL19 MCP-induced oligomerization of SeAvs7 together with EcEF-Tu.

Figure 5

Thirteen additional Avs families are activated by core phage structural and replicative proteins. (**a**) Construction of an expanded plasmid gene library consisting of 600 genes from 36 phages and other viruses, totaling 521 kb of cloned genes. (**b**) Barcode abundance when Avs genes are co-expressed with distinct genes from diverse phages. (**c**) Heatmap of the specificity of Avs7-21 activation by diverse homologs of their cognate target proteins. (**d**) Schematic of the functional roles of phage proteins recognized by Avs families.

Figure 6

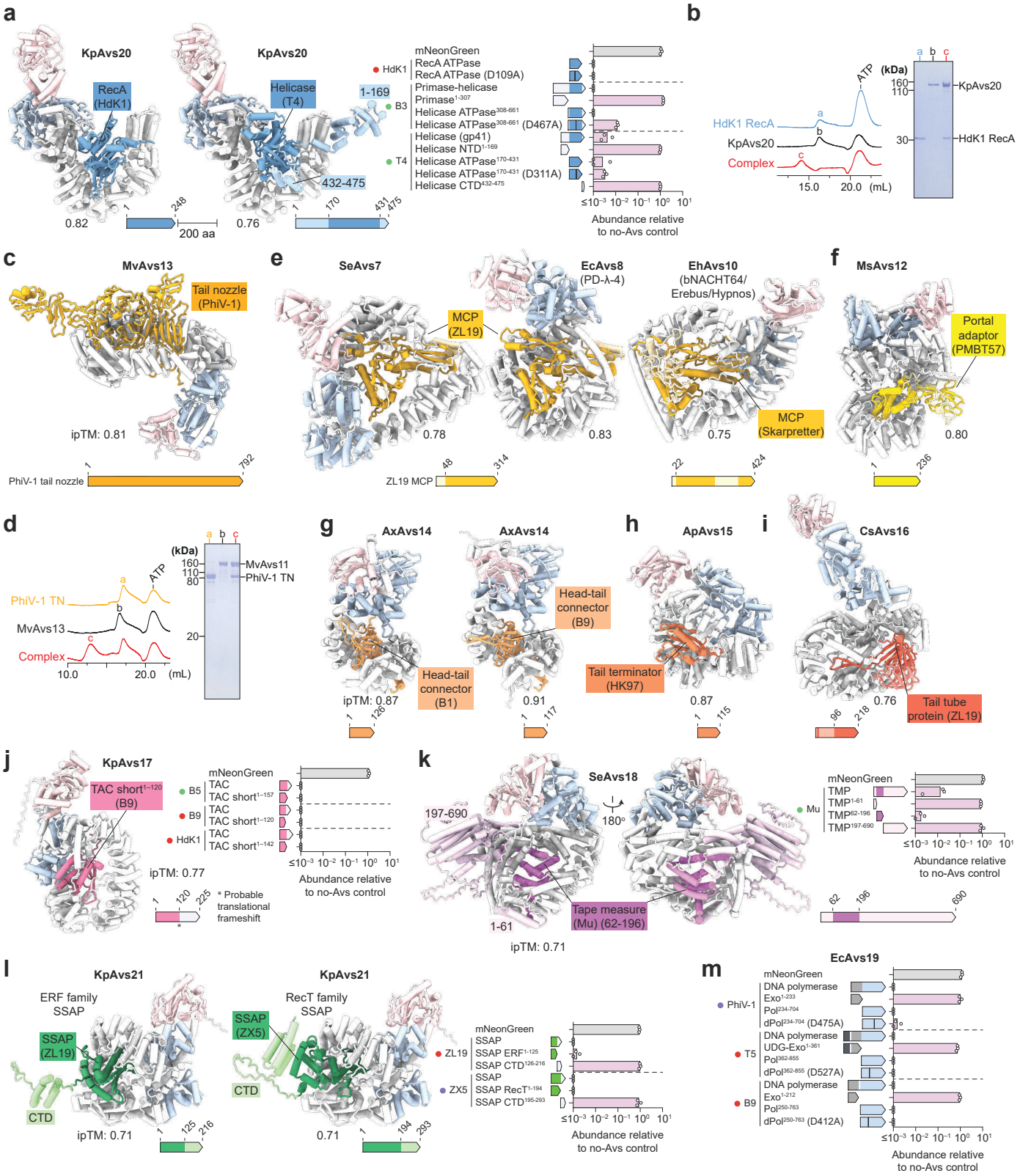

Avs proteins recognize core structural patterns through shape complementarity across extended binding interfaces. AlphaFold2/3 models of Avs proteins binding the (**a**) RecA-fold ATPases, (**c**) tail nozzle, (**e**) major capsid protein, (**f**) portal adaptor, (**g**) head-tail connector, (**h**) tail terminator, (**i**) tail tube protein, (**j**) tail assembly chaperone, (**k**) tape measure protein, and (**l**) ssDNA annealing proteins, accompanied by quantification of Avs activation by truncated or catalytically inactivated target proteins. (**m**) EcAvs19 activation by truncated or catalytically inactivated DNA polymerases. Size-exclusion chromatograms and SDS-PAGE analysis of (**b**) KpAvs20:HdK1 RecA and (**d**) MvAvs13:PhiV-1 tail nozzle complex are shown. ipTM, interface predicted template modeling score (0.0-1.0); TN, tail nozzle.

Figure 7